Mantle melting and intraplate volcanism due to self-buoyant hydrous upwellings from the stagnant slab that are conveyed by small-scale convection

Xiaogang Long[1,2], Maxim D. Ballmer[3,2], Antonio M.-C. Córdoba[2] and Chun-Feng Li[4,5]

[1] School of Ocean and Earth Sciences, Tongji University, Shanghai 200092, China.

[2] Institute of Geophysics, ETH Zurich, Zurich, Switzerland.

[3] Department of Earth Sciences, University College London, London WC1E 6BS, UK.

[4] Department of Marine Sciences, Zhejiang University, Zhoushan 316021, China.

[5] Laboratory for Marine Mineral Resources, Qingdao National Laboratory for Marine Science and Technology, Qingdao 266237, China.

Correspondence to: Xiaogang Long (longxg@tongji.edu.cn)

Key points:

- Intraplate volcanism above stagnant slabs is sustained by interaction of hydrous upwellings and small-scale convection.
- Hydrous upwellings intermittently stall at ~400 km depth before being picked up by small-scale convection.
- Moderate amounts of water in the transition zone (~0.4 wt.-%) are sufficient to trigger volcanism within ~20 Myr.

Abstract

The mechanisms sustaining basaltic continental intraplate volcanism remain controversial. Continental intraplate volcanism is often geographically associated with slab stagnation in the mantle transition zone (MTZ), e.g., in eastern Asia, central Europe, and western North America. Using 2D geodynamic models, we here explore the role of the stagnation of a slab and an associated hydrous layer in the MTZ on the formation and evolution of intraplate volcanism. Due to the intrinsic buoyancy of the hydrous layer atop the stagnant slab, upwellings develop within a few million years and rise to ~410 km depth. At these depths, they partly lose their intrinsic buoyancy due to dehydration, and stall intermittently. However, they are readily entrained by sublithospheric small-scale convection (SSC) to reach the base of lithosphere, sustaining mantle melting and intraplate volcanism. Water contents of >0.3 wt.-% in a ≥60 km thick layer atop the slab are sufficient for an early (< ~20 Myr) onset of melting to account for volcanism, e.g., in NE China. Thus, significant amounts of hydrous materials are not expected to remain stable in the MTZ for geological timescales, consistent with geophysical estimates. To explain the geochemical signatures of the Cenozoic basaltic volcanism in northern China, a mixed composition of the hydrous layer, including an EM-type and a hybrid DMM/HIMU-type component, is required.

1. Introduction

Most of our planet's volcanism occurs near plate boundaries, well explained by plate tectonic processes. In turn, intraplate volcanisms are not readily explained by plate tectonics, but often resort to mantle processes (Morgan, 1971; Wilson, 1973; Tan and Gurnis, 2005; Burke et al., 2008; Ballmer et al., 2015a, 2016)). While the mantle plume theory can explain some major volcano lineaments such as the Hawaii, Iceland and Walvis ridges (Wilson, 1965; Morgan, 1971; O'Connor and Duncan, 1990; Courtillot et al., 2003), numerous exceptions or "non-hotspot volcanism" exist (Batiza, 1982; Okal and Batiza, 1987; McNutt, 1998). Non-hotspot intraplate volcanism is often characterized by (1) non-linear spatial distributions (Kim and Wessel, 2015), (2) non-linear age progressions or linear progressions not consistent with plate motion (e.g., (Ballmer et al., 2009), (3) extended periods of volcanism at a single edifice (Raddick et al., 2002; Garcia et al., 2010; Balbas et al., 2016), or (4) short-lived volcano chains (Clouard and Bonneville, 2005).

Widespread volcanism in the Pacific (e.g., French Polynesia, Darwin Rise) may be related to diffuse mantle upwelling and/or anomalously warm mantle temperatures (McNutt and Fischer, 1987; Staudigel et al., 1991; Bemis and Smith, 1993; Kim and Wessel, 2008; Koppers et al., 2003). Given an initial volcanic load, or distal plate stresses, the lithosphere may crack to trigger new volcanism (Gerbault et al., 1999; Hieronymus and Bercovici, 2000). Rayleigh-Taylor instability in a layer near or at its solidus may induce self-perpetuating decompression melting (Tackley and Stevenson, 1993), which will further fuel the instability (Hernlund et al., 2008) and form short-lived and non-linear volcano chains (Raddick et al., 2002). Small-scale sublithospheric convection (SSC) (Parsons and McKenzie, 1978; Afonso et al., 2008; Dumoulin et al., 2008), caused by the thickening and densification of the thermal boundary layer, can sustain mantle melting and account for seamount chains parallel to plate motion (King and Anderson, 1995; King and Ritsema, 2000; Huang, 2003; Dumoulin et al., 2008), but fails to explain volcanism on thin oceanic plates younger than ~50 Myr (Batiza, 1980; Ballmer et al., 2007). Shear-driven upwelling, excited when horizontal asthenospheric flow interacts with steps in lithospheric thickness (Conrad et al., 2010; Till et al., 2010) or heterogeneities in mantle viscosity (Bianco et al., 2011), can also account for intraplate volcanism in regions of strong mantle flow or shearing (Ballmer et al., 2013).

Similarly, basaltic continental intraplate volcanism has commonly been related to mantle upwelling and decompression melting (Demidjuk et al., 2007; Elkins-Tanton, 2007; Valentine and Hirano, 2010; Conrad et al., 2011), by the same physical mechanisms as beneath oceanic plate described above (Hernlund et al., 2008; West et al., 2009; Kaislaniemi and van Hunen, 2014).

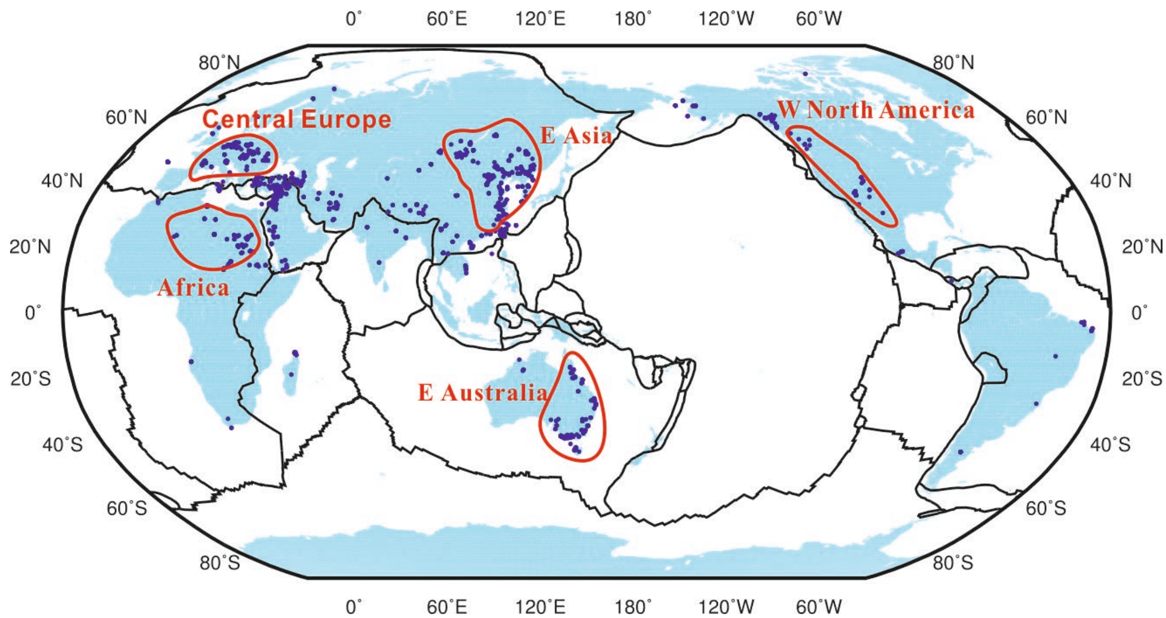

Figure 1. Cenozoic basaltic continental intraplate volcanism (data from GeoRoc: http://georoc.mpch-mainz.gwdg.de/georoc/; filters are "intraplate volcanism" OR "complex settings"). Clusters of enhanced continental volcanism are marked by red closed curves. See also Conrad et al. (2011).

The dominant mechanisms can be assessed by studying global distributions of Cenozoic continental intraplate volcanism, mostly occurring in western North America, central Europe, eastern Asia, eastern Australia and Africa (Figure 1). Except for the basaltic intraplate continental volcanism on the stationary African Plate (Burke et al., 2008), volcanism in other regions can be best explained by non-hotspot volcanism. Western North America and eastern Australia are associated with a rapidly sheared asthenosphere (Conrad et al., 2011). However, most of these regions are also underlain by slabs that stagnate in the mantle transition zone (MTZ). Indeed, seismic tomography (Piromallo and Morelli, 2003; Lei and Zhao, 2005; Zhao and Ohtani, 2009; Schmandt and Lin, 2014), the distribution of seismicity (Fukao et al., 2001; Zhao and Ohtani, 2009), and lava isotope geochemistry (Zou et al., 2008; Kuritani et al., 2011), link slab subduction, stagnation and dehydration to mantle upwelling and intraplate volcanism. For example, Changbai volcano in NE China is inferred to be related to mantle upwelling and melting due to the deep dehydration of the stagnant Pacific slab (Zhao, 2004; Maruyama et al., 2009; Zhao and Ohtani, 2009). The specific geodynamic mechanisms that drive mantle upwelling, however, have not yet been established (Tatsumi et al., 1990; Zhao, 2004; Zhao and Ohtani, 2009). Faccenna et al. (2010) predicted a significant component of poloidal flow around the slab to support diffuse upwelling near the slab tip. However, subducted slabs are expected to primarily induce horizontal toroidal flow (Long and Silver, 2008; Liu and Stegman, 2011; Chen et al., 2016), i.e. with little or no passive upwelling, particularly for a significant viscosity contrasts between the upper and lower mantle (Rudolph et al., 2015).

On the other hand, plume-like self-buoyant upwellings may sustain volcanism above the stagnant slab. For example, the harzburgite layer underlying the basaltic crust of the slab can rise actively through the MTZ, and then be entrained by upper-mantle convection (Motoki and Ballmer, 2015). The initial instability is promoted by the density contrast between the upper and lower part of the slab. Alternatively, the hydrous layer overlying the stagnant slab may undergo convective instability to drive upwelling (Richard and Bercovici, 2009). Hydrous wadsleyite and ringwoodite are positively buoyant (Inoue et al., 2004; Jacobsen et al., 2004; van der Lee et al., 2008), and may hence deliver water to the base of the lithosphere. Such a scenario of continental intraplate volcanism due to hydrous upwellings (Richard and Bercovici, 2009; Richard and Iwamori, 2010) would be analogous to the "cold plumes" proposed by Gerya and Yuen (2004) in mantle wedge. However, previous studies have not addressed the fate of hydrous upwellings as they rise through the mantle and reach the base of the lithosphere to undergo melting. They have also neglected that the layer atop the slab should be already cooled before reaching the MTZ due to thermal diffusion, and the trade-off between this cooling and hydration is expected to control instability.

We here apply two-dimensional numerical models of mantle flow to explore the dynamic mechanisms that sustain intraplate volcanism above a stagnant slab. We carefully compute the initial thermal profile across the slab. In order to predict the spatio-temporal patterns and geochemistry of volcanism, we couple the geodynamic simulations with a melting model for a heterogeneous mantle source. Finally, we compare model predictions with observations to constrain the conditions for mantle upwelling and volcanism. We find that an interaction between (bottom-up) self-buoyant upwelling of a hydrated MTZ and (top-down) SSC is required for intraplate volcanism to occur soon after the slab reaches the MTZ.

2. Methods

2.1 Model setup

In our two-dimensional geodynamic models, we numerically solve the conservation equations of mass, momentum and energy for an incompressible, infinite-Prandtl-number fluid using a Cartesian version of the finite-element code Citcom (Moresi et al., 1996; Zhong et al., 2000; Ballmer et al., 2009). We apply the extended Boussinesq approximations, but neglect shear heating, which has a negligible effect on convection at the given rheology (Zlotnik et al., 2008).

Our model setup is loosely based on Motoki and Ballmer (2015). The two-dimensional model domain is oriented parallel to the trench, just as theirs (see their Figure 1), and our boundary conditions are the same as theirs (Figure 2a). However, our domain is larger than theirs (see below). While our box is mostly bottom-heated with T_0 = 1350 °C imposed at the bottom boundary, we also apply internal heating with radioactive heat production of Q_0 in the mantle. According to our model setup, the initial condition corresponds to the time, at which the sinking slab just reaches the MTZ.

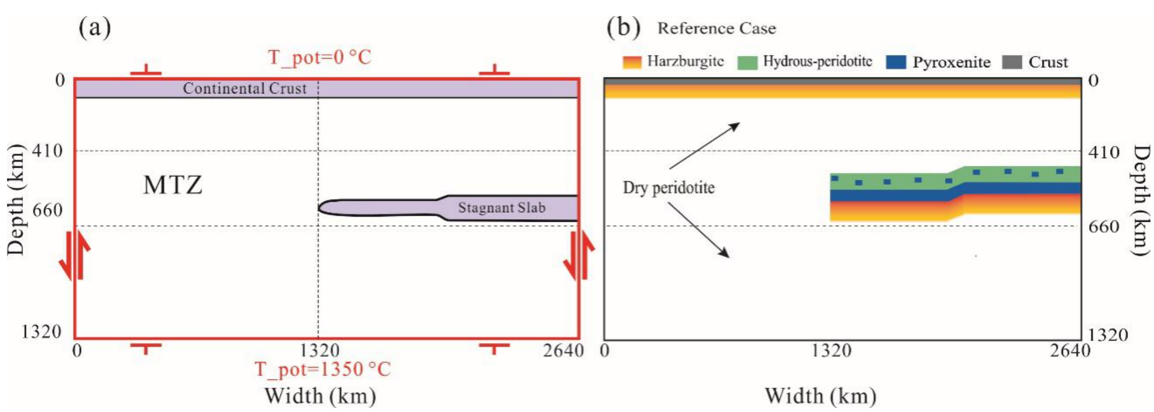

Figure 2. (a) Model setup and initial and boundary conditions. Free slip is applied to left and right boundaries, and no slip to the top and bottom. Potential temperatures are set to 0 °C at the top and 1350 °C at the bottom. (b) Initial composition of the reference case as schematic representation (not to scale). The top grey layer is continental crust (30 km thick). Blue and green colors conceptually show the initial distribution of mafic materials (pyroxenite/basalt) and hydrous peridotite, respectively. The thickness of the pyroxenitic layer near the top of the stagnant slab is 7 km. Small blobs of mafic material are uniformly distributed in the hydrous layer. The thickness of, and the initial fraction of mafic materials in the hydrous layer are model parameters. Yellow-to-orange colors refer to layers of

harzburgite (in the stagnant slab and lithosphere) with a progressive degree of depletion upwards (see text for details). White background colors refer to dry peridotite.

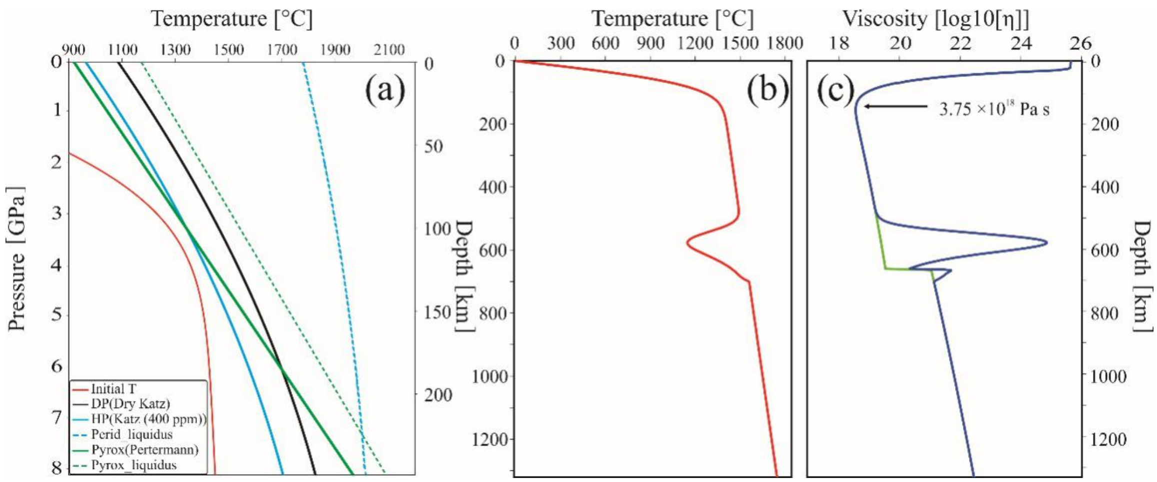

Figure 3. (a) The melting laws applied for depleted peridotite (black) and hydrous peridotite (solid blue line; bulk water content 400 ppm) are from Katz et al. (2003), and melting law for pyroxenite (solid green line) from Pertermann & Hirschmann (2003). Also shown are the liquidus of peridotite (dashed blue line) and pyroxenite (dashed green line), providing a sense for the productivity of each lithology, which is much lower for the former than for the latter lithology. (b) The initial vertical potential temperature profile of all models (i.e., excluding the adiabatic gradient). (c) The initial vertical viscosity profile for the reference case. Blue and green lines represent profiles with and without a slab, i.e. in the right and left parts of the box, respectively. The reference effective viscosity is pointed out by a black arrow.

Our computational domain is 2640 km wide and 1320 km deep (Figure 2). The model is discretized by 1281×481 finite elements in the horizontal and vertical directions, respectively. The grid is uniform horizontally, and a vertical grid refinement improves resolution near the base of the lithosphere and in the MTZ.

The initial condition of temperature involves a slab in the MTZ on top of a background mantle adiabat with a potential temperature of T_0 = 1350 °C. The position and geometry of the slab are shown in Figure 2. Horizontally, the slab is placed in the right half part of the box (1320 ⩽ x ⩽ 2640 km) and consists of two segments with different ages, in between of which a fracture zone is imposed. Vertically, it is placed at an initial position, for which its underbelly (i.e., at a potential temperature of just below 1350 °C) is located at a depth of ~700 km. In our reference case, the slab age is 70 Myr for 1320 ⩽ x < 1980 km and 80 Myr for 1980 ⩽ x ⩽ 2640 km, but these slab ages on either side of the fracture zone are free model parameters. The edge of the slab at x=1320 km is treated like a fracture zone with two adjacent slabs, one of which has a slab age of 0 Myr (i.e., it is non-existent). The initial vertical temperature profile across each slab segment is determined semi-analytically as a function of slab age and slab residence time in the mantle (i.e., assumed to be 10 Myr) according to Motoki and Ballmer (2015) (Figure 3b). At the fracture zones at x=1320 km and x=1980 km, the initial thermal condition does not just include a simple step function, instead, the transition between the two sides of the fracture is well smoothed linearly over a lateral distance of 100 km (see Figure 2a). This is a good proxy for a (thermally healed) fracture zone; for example a subducted fracture zone of age offset ~10 Myr is located in the stagnant slab beneath eastern China (Liu et al., 2017). Finally, on top of the slab, we impose a layer of hydrous material (Figure 2) with a thickness that varies as a free model parameter (see Table 1), independent of the age of the slab.

To account for the overriding plate, we add a thermal profile at the top that corresponds to that of a 50-Myr-old oceanic plate (i.e., according to the half-space cooling model, Figure 3b). This initial thermal profile is a simplified condition for the continental lithosphere, but note that the average thermal profile near the end of the calculations is similar to this condition.

The initial condition of composition consists of three parts (Figure 2): (1) the lithosphere near the top of the model consisting of a ~80 km thick layer of harzburgite, overlain by a 30-km thick continental crust (see below), (2) the stagnant slab in the MTZ consisting of layers of basalt (7 km thick) and harzburgite (~80 km thick) layers, overlain by a hydrous layer of variable thickness, and (3) the ambient mantle consisting of dry peridotite (Figure 2). Note that the hydrous layer contains small blobs of mafic heterogeneity, which may be e.g. originating from the subduction of silicic sediments and hybridization of related melts in the subduction channel (Gerya et al., 2004; Iwamori, 2007). In turn, for the 7-km thick basaltic layer, we have MORB-like materials (and the relevant high-pressure polymorphs) in mind. However, our model results do not depend on any specific assumptions in terms of composition of these mafic lithologies, except for the imposed melting behavior and density profiles (see sections 2.3-2.4). In fact, we consider the same density profile and melting parameterization for both mafic/basaltic materials, considering that both are "pyroxenites"; i.e. the keyword that we use for this lithology hereinafter. We stress that considering any alternative fusible (i.e., high melt productivity) and intrinsically dense lithologies instead of pyroxenites is expected to yield very similar model results.

In turn, harzburgites are not modeled as an independent lithology, but rather as a depleted peridotite. The degrees of depletion of depleted peridotite (DP) and hydrous peridotite (HP), F_{DP} and F_{HP}, increase upwards in each layer (Katz et al., 2003; Ballmer et al., 2009). The explicit profiles of F_{DP} and F_{HP} in each harzburgite layer are pre-calculated from residual profiles of mid-ocean ridge melting (Ballmer et al., 2009), which remains an ad-hoc simplification for the sub-continental layer. Likewise, the continental crust is also modeled as depleted peridotite (with $F_{DP} = F_{HP} = 0.2$ in the 30-km thick crustal layer) and not as an independent lithology. Accordingly, the intrinsic buoyancy of the continental crust is just ~33 kg/m^3 (see eq. 2 below). While such a small anomaly remains a very conservative choice, it is sufficient to guarantee stability of the crust (also because the crustal layer is within the strongest part of the lithosphere). Along these lines, we really just model a mix of three lithologies: dry (depleted) peridotite (DP), hydrous (enriched) peridotite (HP), and pyroxenites (PX).

In the reference case, 2 wt.-% pyroxenites (Figure 2) are mixed into a 40 km thick hydrous layer. The hydrous layer is meant to represent a layer in the transition zone that is enriched in volatiles and pyroxenites through the long-term subduction (and accumulation) of a hydrated mélange (+silicic sediments) through a channel atop the slab (Gerya et al., 2004; Iwamori, 2007; Marschall and Schumacher, 2012), or formed by the long-term delivery of water that transported to the MTZ in the cool sinking slab (and continuous dehydration in the MTZ) (Frost, 2006).

2.2 Rheology parameterization

In a conservative approach, we use a simplified Newtonian rheology to model mantle flow:

$$\eta = \lambda_i \eta_0 exp(-\frac{E^*+pV^*}{RT} + \frac{E^*}{RT_0}), \quad (1)$$

with η viscosity, η_0 the reference viscosity calculated for zero pressure and $T = T_0$, λ_i a depth-dependent viscosity pre-factor, E^* activation energy, V^* activation volume, R the ideal gas constant, p pressure, T temperature, and T_0 the reference temperature. In the resulting viscosity profile (Figure 3c), we define η_{eff} as the effective viscosity (i.e. the minimum viscosity of the asthenosphere at time-step zero). We consider a relatively low activation energy of $E^* = 200$ *kJ/mol* in order to mimic the composite effects of dislocation and diffusion creep in a simplified Newtonian-rheology description (Christensen, 1984; van Hunen et al., 2005). Our simplified rheology is just temperature-dependent and depth-dependent due to our choices of E^*, V^* and λ_i. We apply λ_i of 1 and 30 for above 660 km and below 660 km, respectively. Accordingly, at 660 km depth, a viscosity jump of factor 30 is imposed (Figure 3c) (King and Masters, 1992; Peltier, 1996; Mitrovica and Forte, 1997; Kaufmann and Lambeck, 2000).

248 **Table 1**: Governing Parameters

Parameter	Description	Value or Range
c_p	Specific heat capacity	1250 $J/kg \cdot K$
E^*	Activation energy	200 kJ/mol
V^*	Activation volume	4×10^{-6} m^3/mol
Q_0	Internal heating	9.995×10^{-12} W/m^3
g	Gravitational acceleration	9.8 m/s^2
L	Latent heat of melt	5.6×10^5 J/kg
T_0	Reference temperature	1350 $^\circ C$
α	Thermal expansivity	[a]
γ	Adiabatic gradient	0.3 K/km
Γ	Clausius-Clapeyron slope at 660 km	-3×10^6 MPa/K
$\Delta\rho_{depl}$	Density anomaly related to 100% depletion	-100 kg/m^3
$\Delta\rho_{melt}$	Density anomaly related to 100% melt	-500 kg/m^3
$\Delta\rho_{PX}$	Density anomaly related to 100% pyroxenite	91.15 kg/m^3
$\Delta\rho_{H_2O}$	Density anomaly related to 100 ppm water	-0.5 kg/m^3 [b]
η_{eff}	Effective mantle viscosity	2.2×10^{18}-1.1×10^{19} $Pa \cdot s$
κ	Thermal diffusivity	1×10^{-6} m^2/s
ρ_0	Reference mantle density	3300 kg/m^3
ρ_ϕ	Magma density	2800 kg/m^3
ϕ_c	Critical porosity	0.1 %
C_{H2O_DP}	Water content of dry peridotite	400 *wt.-ppm*
C_{H2O_HP}	Water content of hydrous peridotite	400-10000 *wt.-ppm*
D_{HP}	Thickness of the hydrous layer	20-135 km
χ_i	Mass fraction of a lithology (i = [DP,HP,PX])	$\chi_{DP}+\chi_{HP}+\chi_{PX}=1$

249 [a] Depth-dependent based on (Tosi et al., 2013); see text.

250 [b] From (Inoue et al., 1998; Angel et al., 2001; Wang et al., 2003; Panero, 2010).

251

2.3 Melting parameterization

To model mantle melting, we consider three different components in the mantle source (Figure 2): dry peridotite, hydrous peridotite and pyroxenite (again, harzburgite is not an independent lithology; see above). We use a relatively simple model of melting, melt migration and melt extraction to efficiently model magma generation in the upper mantle. For example, we do not explicitly account for porous flow of magma, but rather consider melt extraction based on the dynamic melting approximation (McKenzie, 1985; Elliott, 1997; Schmeling, 2006). Magma is immobile until the critical porosity φ_C is reached in the peridotite mineral assemblage. Magma is instantaneously extracted to the surface once the melt fraction exceeds φ_C, assuming that the timescale of melt migration and extraction is much smaller than of mantle flow (Kelemen et al., 1997). We choose a critical porosity of $\varphi_C = 0.1$ % (Stracke et al., 2006), at which (hydrous) melts form an interconnected network (Mei et al., 2002), and are efficiently extracted, particularly in deformed aggregates (Holtzman et al., 2003). Melting is treated as a semi-reversible process, in which refreezing of any retained magma back to peridotite or pyroxenite occurs as soon as temperature decreases or pressure increases. Latent heat of melt is consumed in the melting process and released in the refreezing process.

We consider melting laws of Katz et al. (2003) and Pertermann & Hirschmann (2003) for the melting of peridotite and pyroxenite, respectively (Figure 3a). However, we restrict any melting beyond a cutoff of 8.05 GPa (~250 km); the melting parameterizations are not valid for any higher pressures, and we do not expect any melting there (Andrault et al., 2018). In any case, as no melting in our models happens at pressures larger than ~4 GPa (see results section), our results are not sensitive to our choice of the cutoff. The effects of water on depressing the solidus of peridotite is self-consistently accounted for (Ballmer et al., 2009).

2.4 Density parameterization

Flow in the model is driven by mantle buoyancy, which is affected by thermal and compositional density anomalies. Density ρ is a function of temperature T and composition modified by melting and refreezing processes, depth and water content:

$$\rho = \rho_0[1 - \alpha(T - T_0)] - \Delta\rho_{melt}(\chi_{DP}\varphi_{DP} + \chi_{HP}\varphi_{HP} + \chi_{PX}\varphi_{PX}) + \beta\Delta\rho_{PX}\chi_{PX}$$
$$-\beta\Delta\rho_{depl}(\chi_{DP}F_{DP} + \chi_{HP}F_{HP}) - \Delta\rho_{H_2O}(\chi_{DP}C_{H_2O\_DP} + \chi_{HP}C_{H_2O\_HP}), \quad (2)$$

where ρ_0 is the reference density, T and T_0 are the temperature and reference temperature, respectively. α is the thermal expansivity, $\Delta\rho_{\mathrm{melt}}$ and $\Delta\rho_{\mathrm{depl}}$ are the density changes due to melt and depletion, respectively. χ_i and φ_i are the mass fractions and porosities (i.e., magma fractions), respectively, of a given lithology i (i = [DP, HP, PX]). $\Delta\rho_{\mathrm{PX}}$ is the excess density of pyroxenites, $\Delta\rho_{\mathrm{H2O}}$ is the density change due to the presence of water in nominally anhydrous minerals, and C_{H2O_DP} and C_{H2O_HP} are the water contents in dry and hydrous peridotite, respectively. α is depth-dependent based on (Tosi et al., 2013), varies linearly from 4.5×10^{-5} K^{-1} at the surface to 2.1×10^{-5} K^{-1} at 660 km depth, and fixed at 2.2×10^{-5} K^{-1} below 660 km depth. $\Delta\rho_{\mathrm{depl}}$ and $\Delta\rho_{\mathrm{PX}}$ vary with depth, and β is the depth-dependent pre-factor that we use to parameterize this behavior (Hirose et al., 1999; Aoki and Takahashi, 2004; Xu et al., 2008):

$$\beta = \begin{cases} 1.65, & if \quad 0 \ll z < 300\ km \\ 2.30, & if\ 300 \ll z < 410\ km \\ 1.00, & if\ 410 \ll z < 660\ km \\ -1.75, & if\ 660 \ll z < 730\ km \\ 1.16, & if\ 730 \ll z \ll 1320\ km \end{cases}$$

Finally, we consider the effect of phase change at 660 km depth on buoyancy according to Ballmer et al. (2015), using a Clausius-Clapeyron slope of $\Gamma = -3.0$ MPa/K (Ito and Takahashi, 1989).

2.5 Dehydration of hydrous peridotite at the 410 km discontinuity

In our model, the initial water content of hydrous peridotite in a hydrous layer on top of the slab (Figure 2) is taken to vary between 400 and 10000 wt.-ppm (or 0.04 to 1 wt.-%). These are conservative bounds considering the high water solubility of ringwoodite and wadsleyite (Ohtani et al., 2004; Pearson et al., 2014), and the different ways of water transport to the MTZ (Faccenda et al., 2009; van Keken et al., 2011; Nishi et al., 2014; Ohira et al., 2014) (see section 4.4). In contrast, the water content above 410 km depth is limited to 400 wt.-ppm (Férot and Bolfan-Casanova, 2012). In order to take into account the dehydration of any excessive water in the upwelling mantle at 410 km depth due to the stabilization of a supercritical-fluid layer (Bercovici and Karato, 2003), we use a crude ad-hoc approach of removing the excessive water from the model. We assume that the water remains in the gravitationally-stable supercritical-fluid layer instead of diffusing into uppermost mantle (for further discussion, see below).

3. Results

3.1 General model predictions: the reference case

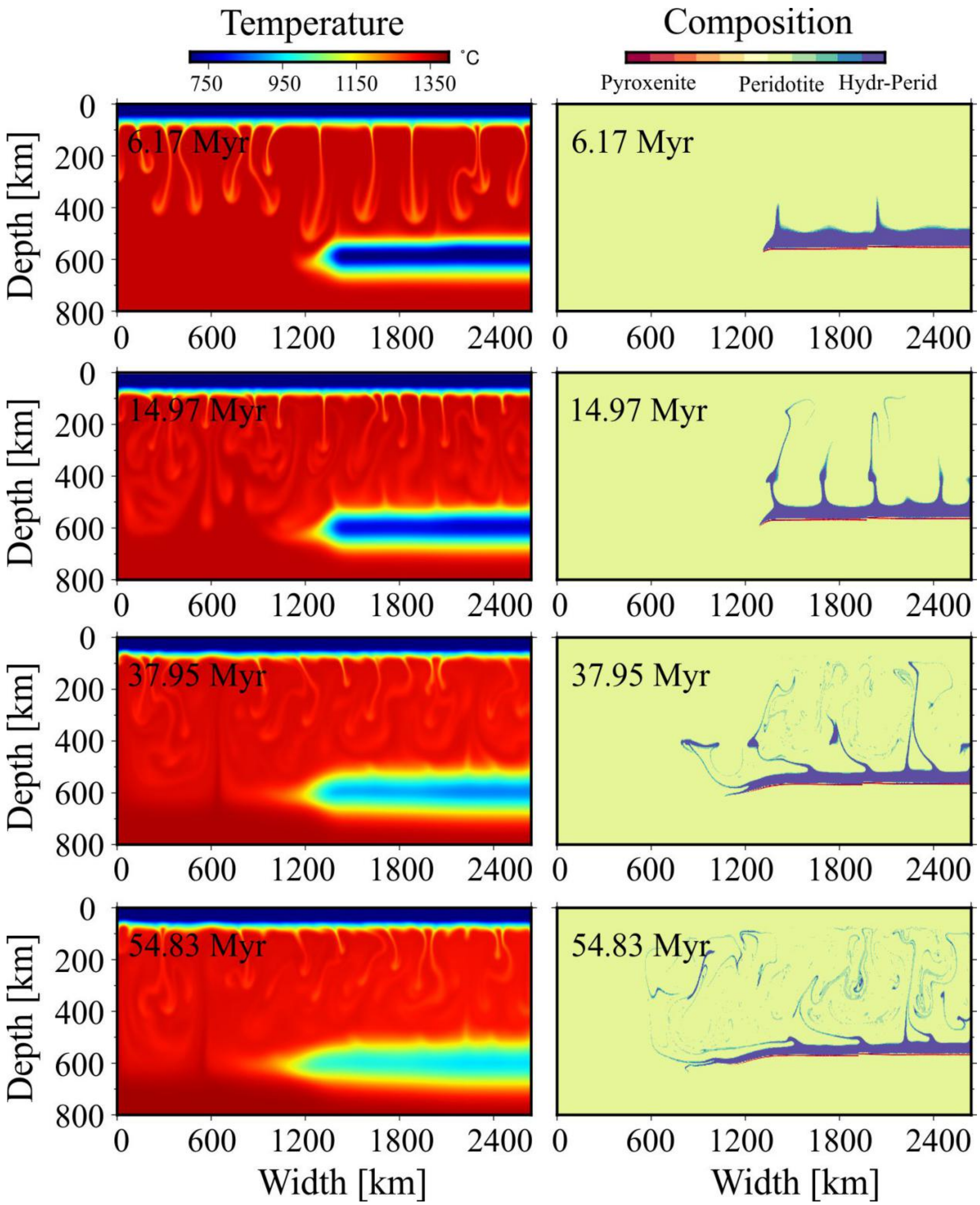

Figure 4. Time series with snapshots of temperature (left) and composition (right) for the reference case.

In our suite of numerical models, we find a typical evolution of thermochemical convection and related mantle melting for a wide range of parameters. We first establish this robust behavior by describing in detail the model predictions of our reference case. The governing parameters of this reference case are $\eta_{eff} = 3.75\times10^{18}$ $Pa{\cdot}s$, $C_{H2O\_HP} = 4000$ wt.-ppm and $D_{HP} = 60$ km (for additional parameters, which mostly remain fixed across model suite, see Table 1) (for initial model setup see Figure 2).

Figure 4 shows the temporal evolution of temperature (left) and composition (right) of the reference case. The related density variations that drive the flow are shown in Figure 5; associated mantle melting and volcanism are presented in Figure 6. In Figures 4-5 and 6, only the upper 800 km and upper 150 km, respectively, of a model box with vertical extent of 1320 km, are shown.

The initial model setup represents the beginning of the stagnation phase of the slab, i.e. just after the end of slab sinking through much of the upper mantle. In the very beginning of the simulation, the slab still sinks a bit until it settles at a depth of 600~700 km (within a couple of Myr of model time), floating at the 660 km discontinuity due to the downward deflection of the related phase transition and related buoyancy force (Figure 5, the positive buoyant (red) part of the slab). At the same time, the very first self-buoyant upwellings develop at the slab tip and near the imposed fracture zone from a hydrous layer atop the slab. The hydrous layer in the reference case contains 2% of mafic materials (or pyroxenites) in addition to hydrous peridotite. These self-buoyant upwellings are driven by a density inversion of hydrated peridotite (Figure 5), and triggered early in the simulation due to the lateral heterogeneity provided by the fracture zone, or at the slab tip (Huang et al., 2003; Dumoulin et al., 2004).

During the onset of upwellings, SSC develops at the base of the continental lithosphere, and reaches ~410 km depth at ~5 Myr. Active hydrous upwellings reach these depths soon after that. Meanwhile, the slab is heated by the ambient mantle, which further promotes convective instability. As a result, upwellings begin to develop not only at the slab tip or fracture zone but also between them at ~10 Myr.

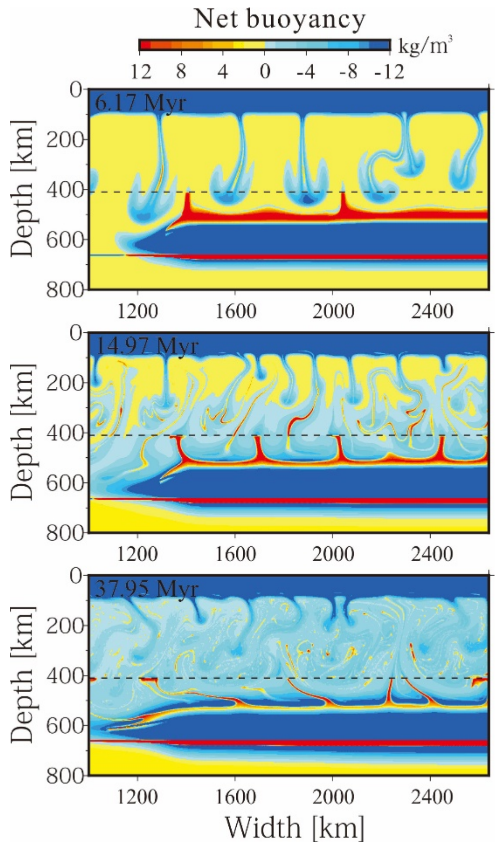

Figure 5. Map of densities ρ (see eq. 2) of the reference case for three snapshots (as labeled). Colors represent total (i.e., thermal plus compositional) density anomalies, or "net buoyancy" (warm colors: positive buoyancy or negative total density anomaly; cold colors: negative buoyancy or positive total density anomaly). The 410 km discontinuity, where much of the buoyancy related to hydration of peridotite is lost, is marked by a black dashed line. The ages of the slab when subducted at the trench are 70 Myr on the left and 80 Myr on the right side of the fracture zone, respectively.

As the self-buoyant upwellings ascend through the upper mantle, they encounter the phase transition at 410 km depth, where minerals are dehydrated, and partly lose their intrinsic buoyancy. Figure 5 shows the net buoyancy, which includes thermal and compositional buoyancy, of the model at three time steps corresponding to the first three panels of Figure 4. The first panel clearly shows that the buoyancy of the upwellings mostly comes from the material in the core of the upwelling (red part), which is hydrous peridotite. Because the water content of hydrous peridotite in the reference case (4000 wt.-ppm) is higher than the capacity of the mantle above 410 km depth (400 wt.-ppm according to our parameterization), much of the water within the upwellings is lost (or left behind) in this case (and most other cases modeled), e.g. to stabilize a melt layer (see discussion below). Since the water in anhydrous minerals provides most of the buoyancy for the otherwise negatively buoyant (cool) upwellings, upwellings tend to stall near 410 km depth (Figures 4 and 5) forming a layer of mostly hydrous material (Figure 4). This stagnant layer is ultimately passively entrained by SSC cells. In other words, self-buoyant upwellings from bottom-up driven instability of the hydrous layer intermittently stall just above the MTZ due to loss of H_2O, but are readily passively entrained by top-down driven convective instability.

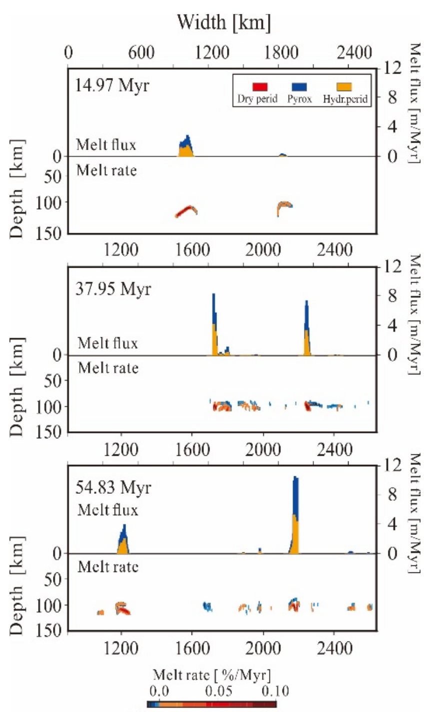

Figure 6. Snapshots of melt flux and melting rate. In the bottom inset of each panel, melting rate in the uppermost mantle is shown (colors). The vertical scale is inflated for visibility. In the top of each panel, the resulting cumulative melt flux is shown with colors representing source lithology. The melt flux is calculated from the cumulated extracted melt volume (i.e., the melt fraction that exceeds the critical porosity) from the underlying column of mantle rocks.

As being passively entrained and carried by the SSC cells, hydrous material eventually reaches the base of the lithosphere. The presence of volatiles in the hydrous material significantly reduces the solidus temperature to allow (partial) decompression melting within the entrained hydrous blobs. The small fraction of fertile pyroxenites in the hydrous material contributes significantly to mantle melting. First melting occurs at ~11.8 Myr model time (not shown in Figures, see supplemental Table S1), and increases in vigor through the next few Myr as more and more hydrous material reaches the base of the lithosphere. Partial melting takes place at ~100 km depth, and primarily in a region directly above the slab. Melting further increases in vigor as the accumulation of hydrous material near 410 km depth is progressively entrained by the SSC (Figure 4). Degrees of melting in hydrous peridotite and pyroxenites reach ~5.0% and 38%, respectively. Any melt fractions exceeding the critical porosity of 0.1% are extracted and assumed to contribute to volcanism. Extracted magmas are sourced by mantle melting of hydrous peridotite and of pyroxenites to about equal parts (~55:45). The temperature of the upper (most) mantle decreases continuously as more and more cool hydrous materials are delivered by SSC. Additionally, melting also consumes latent heat and contributes to the cooling of the upper mantle, eventually hampering any further melting.

3.2 Parameter study

In order to further explore the origin of the spatial and temporal patterns of intraplate volcanism above the stagnant slab, key model parameters are varied to investigate their effects on the onset time of upwelling (τ_u), onset time of melting (τ_m), "pyroxenite contribution" (or fraction of pyroxenite-derived magmas in volcanism), and cumulative extracted melt volumes within 70 Myr (Figure 7). τ_u is defined as the time when the first upwelling from the slab reaches 450 km depth; τ_m is the time when partial melting first occurs at the base of the lithosphere. The model parameters that we explore include the viscosity of the asthenosphere (η_{eff}), water content(C_{H2O_HP}), thickness of the hydrous layer (D_{HP}), initial pyroxenites fraction in the hydrous layer (χ_{PX}), and the plate ages at trench on both sides of the slab.

3.2.1 Effective viscosity

In our models, the timing and dynamics of self-buoyant upwellings from the top of the slab strongly depends on η_{eff}. The hydrous layer at the top of the slab, from which the upwellings rise, is somewhat warmer and less strong that the core of the slab. The relevant local viscosity is 10~100 times higher than, but directly coupled to, η_{eff}. The same holds true for the viscous layer at the base of the lithosphere, out of which SSC instabilities develop (e.g., (Liao et al., 2017)). Both Rayleigh-Taylor instability in the hydrous layer, and SSC instability at the base of the lithosphere is controlled by the local viscosity. Thus, τ_u and ultimately τ_m are expected to be controlled by η_{eff}.

In our study, we vary η_{eff} from 2.2×10^{18} to 1.1×10^{19} $Pa{\cdot}s$. As expected, the dominant effect of increasing η_{eff} is to delay convective instability and related melting (Figure 7a and d). Also, for higher η_{eff}, convection and melting are less vigorous (Figure 7j). In turn, pyroxenite contribution remains mostly robust as long as $\eta_{eff} \leq 8.8\times10^{18}$ $Pa{\cdot}s$ (Figure 7g). Small $\eta_{eff} \leq 6.25\times10^{18}$ $Pa{\cdot}s$ are associated with $\tau_m < 20$ Myr (Figure 7d). For these cases, the compositional fingerprint of related lavas also remains robust, as measured by pyroxenite contributions of ~50%. That said, cases with $\eta_{eff} \leq 2.2\times10^{18}$ Pa·s display minor contributions (up to ~12%) of DP-melting.

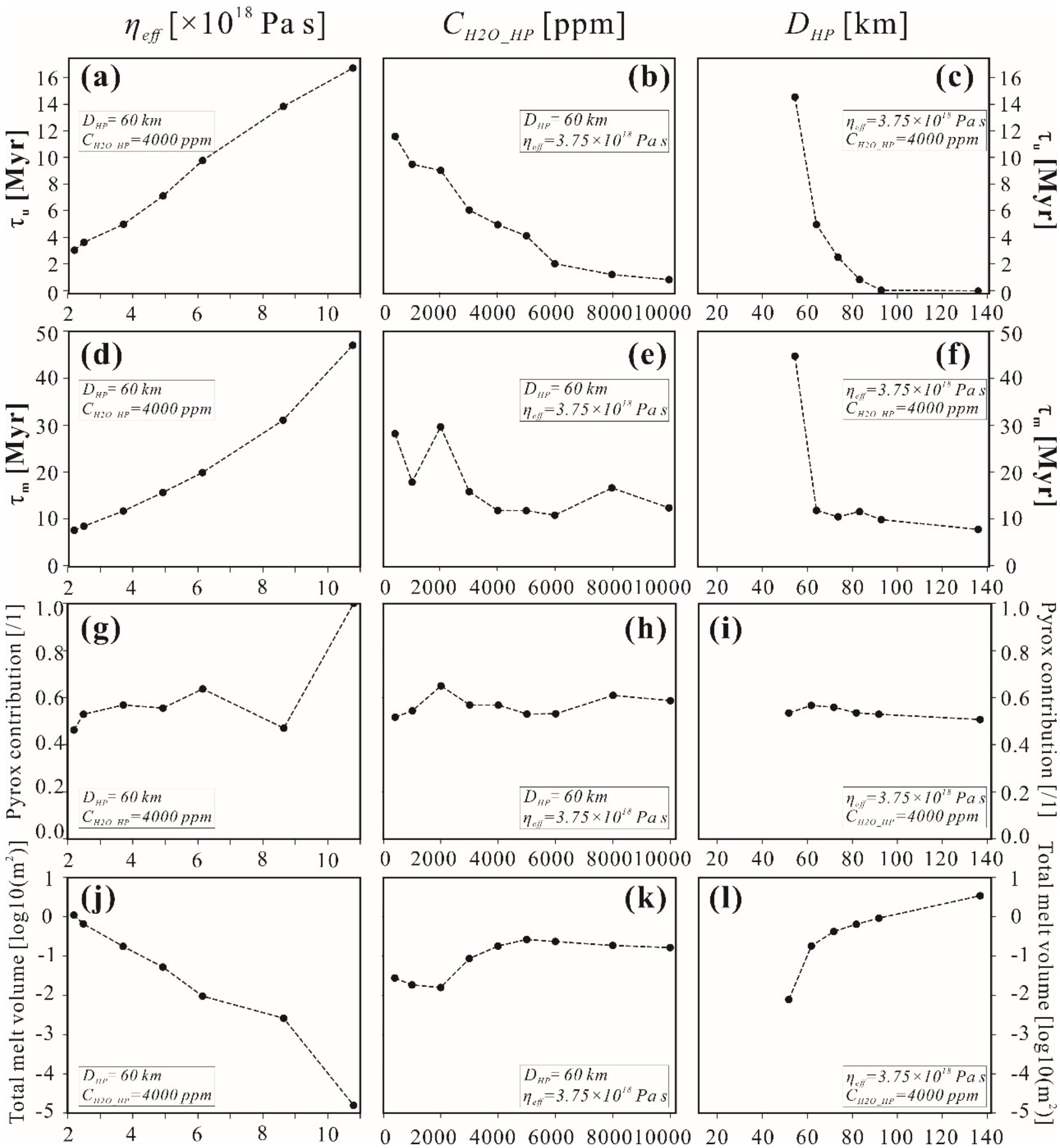

Figure 7. The effects of model parameters η_{eff}, C_{H2O_HP} and D_{HP} (as labeled) on the onset time of upwelling (a-c), onset time of melting (d-f), pyroxenite contribution to volcanism (g-i) and total melt volume extracted (j-l). Melt volumes are cumulative extracted volumes over model times ≤70 Myr. The other two key model parameters are provided in the insets. If no circle and related line(s) are plotted in panels (c), (f), (i) and (l), no upwelling or melting occurs in the corresponding model, respectively (Supplemental Table S1).

3.2.2 Bulk water content

Increasing the bulk water content C_{H2O_HP} decreases the intrinsic density of the hydrous peridotite layer. In other words, the presence of water provides buoyancy to hydrous materials, thus promoting upwellings from the slab. Accordingly, we expect that increasing C_{H2O_HP} tends to advance both upwelling and melting.

Indeed, our models predict that τ_u systematically decreases with increasing C_{H2O_HP} (Figure 7b). In general, τ_m decrease with increasing C_{H2O_HP} as long as $C_{H2O\_HP} < 4000$ wt.-ppm. However, for $C_{H2O\_HP} \geq 4000$ wt.-ppm, τ_m and total volumes of melting remain virtually constant. This prediction is mostly explained by the upper limit of 400 wt.-ppm water in olivine. Even though upwellings are develop rather early for these cases, it still takes ~10 Myr for hydrous materials to travel from top of the MTZ to the base of lithosphere. Besides, pyroxenite contribution to volcanism is virtually independent of C_{H2O_HP}, demonstrating that 2% pyroxenite in the hydrous layer is able to give rise to a nearly 50-50 mixed source of volcanism for a wide parameter range.

3.2.3 Thickness of hydrous peridotite

The thickness of the hydrous-peridotite layer is one of the key parameters to control the rise of hydrous upwellings from the slab, and related volcanism. Its primary effect on τ_u and τ_m is similar to that of C_{H2O_HP}. τ_u and τ_m generally decreases with increasing thickness of the hydrous layer, well understood from a Rayleigh-Taylor stability analysis. As shown in Figure 7c and f, the results can be divided into three regimes. For $D_{HP} \leq 40$ km, there is no upwelling and hence no melting within 70 Myr (not shown in Figure 7 (c), (f), (i) and (l)). For $40 < D_{HP} < 90$ km, upwelling and related melting are systematically advanced as D_{HP} increases. This effect is explained by an increase in positive buoyancy related to hydration in the layer above the slab. Finally, for $D_{HP} \geq 90$ km, the effect of D_{HP} on τ_u and τ_m is negligible.

3.2.4 Initial pyroxenite fraction in the hydrous layer

To explore the effects of the initial fraction of pyroxenite (χ_{PX}) in the hydrous (HP) layer, we vary this fraction between 0.0% and 5.0%. χ_{PX} has a strong influence on pyroxenite contribution to volcanism, and can also affect τ_u through its direct effect on the buoyancy of the hydrous layer. As pyroxenite is intrinsically dense, this buoyancy should decrease with increasing χ_{PX}. Accordingly, τ_u is expected to increase with increasing χ_{PX}.

Figure 8 shows the effects of χ_{PX} on τ_u, total melt volume and pyroxenite contribution. τ_u only increases from 4.5 to 6 Myr as χ_{PX} increases from 0.0% to 5.0%. As expected, pyroxenite contribution is strongly sensitive to χ_{PX}, increasing systematically from 0% to about 80% as χ_{PX} increases from 0.0% to 5.0%. Accordingly, geochemical signatures of related magmas may be used to constrain the initial pyroxenite content in the hydrous layer above the slab (Figure 8). In turn, the effects of χ_{PX} on total melt volumes remain small, because increasing χ_{PX} not only promotes melting, but also decreases the vigor of upwelling and makes hydrous material more difficult to be entrained by SSC. Because of this same trade-off, τ_m remains mostly robust at ~12 Myr with increasing χ_{PX} (not shown in Figure 8, see supplemental Table S1).

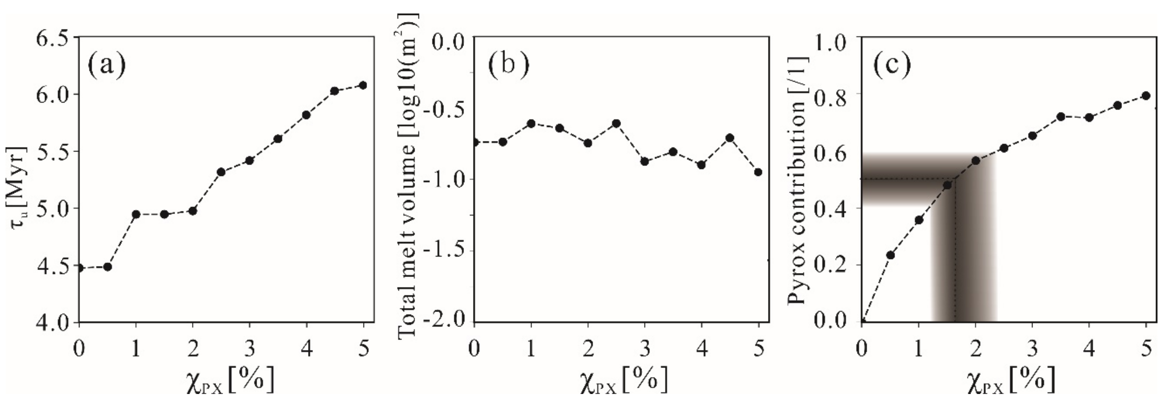

Figure 8. The onset time of upwelling τ_u (a), total melt volume (b) and pyroxenite contribution (c) versus initial fraction of pyroxenite within the hydrous layer (χ_{PX}). Shadow in (c) marks the range of pyroxenite contributions between 0.4 and 0.6, which are most consistent with the geochemical signatures of Cenozoic intraplate volcanism in eastern China, and the corresponding constraints on parameter χ_{PX}.

3.2.5 Heterogeneity within stagnant slab

In all our models, first upwellings rise from the slab tip, and near the fracture zone within the slab (Figure 4). These predictions imply that lateral heterogeneity can trigger the ascent of hydrous plumes, analogous to the well-understood advancement of SSC by lateral heterogeneity (King and Ritsema, 2000; Huang et al., 2003; Dumoulin et al., 2004). In all the cases discussed so far, the imposed age jump at the fracture zone is fixed at 10

Myr; the age at trench of the left section (1320 < x <1980 km) of the slab is 70 Myr, and that of the right section (1980 < x <2640 km) is 80 Myr. To explore the effects of the age of the subducted slab and of the imposed age jump, two groups of cases with different configurations are investigated.

In the first group (Figure 9 (a) and (b)), no age jump is imposed, but the age of the slab at trench (i.e. when the plate was subducted at 10 Myr before the start of the model) is systematically varied. In all these cases, the first upwelling appears at the slab tip. For small slab ages, τ_u first slightly increases with slab age and then remains nearly constant. For large slab ages, τ_u systematically decreases from ~6 to ~4.8 Myr. In contrast, the total volumes of melting decrease systematically with slab age. The predicted trends for small slab ages (<30 Ma) are well explained by the decrease of available net buoyancy within the hydrous layer that drives Rayleigh-Taylor instability with increasing slab age. Higher slab ages imply lower temperatures of the slab and the overlying hydrous layer, which leads to a later onset of upwellings, a smaller portion of the hydrous layer to become convectively unstable, and eventually less melting at the base of the lithosphere. However, higher slab ages also lead to shorter distance between hydrous layer and 450 km depth, where τ_u is measured. Moreover, as slab ages increase, the heterogeneity at the slab tip also becomes stronger, driving earlier instability. These two effects trade off with the above buoyancy effect in terms of τ_u, eventually resulting in earlier upwellings but smaller melt volumes as slab ages increase.

In the second group (Figure 9(c) and (d)), we investigate the effects of the age jump at the heterogeneity within the slab. We fix the slab age of the left section at 70 Myr, and vary the slab age of the right section between 60 and 80 Myr. Hence, we implicitly vary the age jump across the modeled subducted fracture zone. The flat curve in Figure 9c (black line) implies that early upwelling (τ_u = ~5 Myr) develops at the slab tip regardless of the fracture-zone age jump, and allows significant mantle melting. Thus, our results are mostly robust and virtually independent of the age jump. We note, however, that the onset age of instability that rises from near the heterogeneity does indeed depend on the age jump, and big age jumps promote local upwelling (see blue line in Fig. 9c). Thereby, the location of upwelling instability and related distribution of magmatism depends on heterogeneity in the MTZ. Also, the total volume of volcanism increases as a larger portion of hydrous material rises sufficiently early, e.g. near the fracture zone.

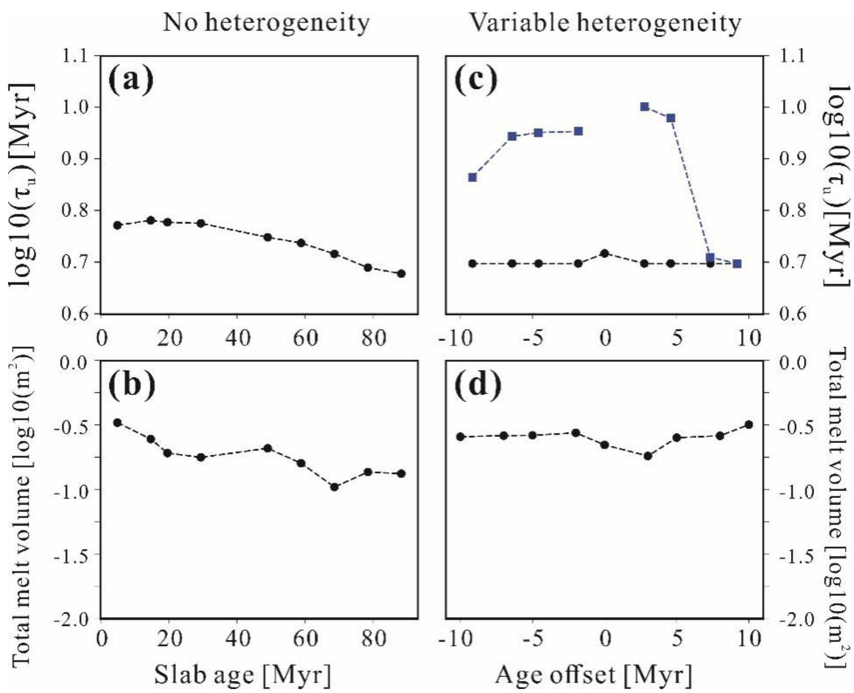

Figure 9. The effects of "slab ages" (i.e. plate ages at trench) on both sides of the fracture zone on model results in terms of τ_u ((a),(c)) and total melt volumes ((b),(d)). No fracture zone is imposed within the slab in (a) and (b). A fracture zone with a variable age offset (as labeled) is imposed in (c) and (d). The age of the left side of the slab is fixed at 70 Myr. The blue line denotes the onset age of instability from near the fracture zone, which is delayed compared to upwelling from the slab tip (black line) in (c).

Heterogeneity within subducted slabs (e.g., slab tears or slab window) are widely detected (Dickinson and Snyder, 1979; Thorkelson, 1996; Miller et al., 2006; Rosenbaum et al., 2008; Cao et al., 2014; Windley and Xiao, 2018). Specifically, a subducted fracture zone of age offset ~10 Myr is located on the subducted Pacific slab beneath eastern China (Liu et al., 2017). Note that slab tears or slab windows may even have a larger effect on the onset of instability than fracture zones with an offset of ~10 Myrs such as modeled here.

3.2.6 Initial distribution of pyroxenite

To better understand the effects of the initial distribution of pyroxenite through the mantle, three different initial conditions are explored here. In group A (made up by all models discussed above; see cartoon in Figure 2b), a minor fraction of pyroxenite (0.0-5.0 wt.-%) is initially distributed through the hydrous layer, but not through the ambient mantle. In group B (cartoon: Suppl. Fig.1a), pyroxenite is initially neither distributed through the ambient mantle nor through the hydrous layer. In group C (cartoon: Suppl. Fig.1b), a minor fraction of pyroxenite (0.1 % or 1.0 wt.-%) is initially distributed through the ambient mantle, but not the hydrous layer; the ambient mantle is further assumed to contain 2.5 wt.-% hydrous peridotite. As in group A, we also explore the same parameter space but with larger steps for groups B and C. Indeed, the distribution of mafic lithologies (e.g., MORB and pyroexnites) remains poorly understood (Nakagawa and Buffett, 2005; Brandenburg and Keken, 2007; Ballmer et al., 2015a). Over geologic time, subducted MORB and other flavors of pyroxenites have been stirred through the mantle (Weaver, 1991; Hanyu and Kaneoka, 1997; Kogiso et al., 1997).

In group B, hydrous materials are also transported by upwelling from the MTZ to the base of the lithosphere, and sustain magmatism there. However, the produced melt only originates from hydrous-preidotite melting. Except for that, results of group B are very similar to group A.

In group C, volcanism is instead mainly sourced by pyrosenite (PX)-melting (mostly $\geq$ 90%), even if the initial fraction of PX is very small (χ_{PX} = 1%). Magmatism occurs everywhere in the asthenosphere and not just above the stagnant slab. Thus, if volcanism is indeed focused in regions that are underlain by a stagnant slab, enriched pyroxenitic/mafic heterogeneity needs to be located in a buoyant hydrous layer atop the slab (i.e., as in group A), and not just in the MORB layer (group B) and not everywhere (group C).

Model predictions in terms of pyroxenite contribution to magmatism strongly vary between groups, thus being sensitive to the initial condition. In group A, pyroxenite contributions are around 50% for all cases with $\eta_{eff} \leq 8.8\times10^{18}$ Pa·s (Figure 7). In group B, pyroxenite contributions are nearly zero. In other words, pyroxenite from the 7 km thick pyroxenitic layer of the recently subducted stagnant slab does not get entrained by the hydrous plumes to rise to the base of the lithosphere in this group (and all of our models). In group C, pyroxenite contributions are strongly sensitive to χ_{PX}. Because of high melt productivity of pyroxenite (Figure 3a), only χ_{PX}= 0.1 wt.-% in the ambient mantle are able to yield pyroxenite contributions of ~64%. Maybe a lower χ_{PX} can result in a pyroxenite contribution 50%, consistent with geochemical signatures of Cenozoic intraplate volcanism in eastern China as discussion below. However, these low χ_{PX} are smaller than those estimated from the inversion of MORB melting (Hirschmann and Stolper, 1996). In any case, the extents of melting of mafic materials (pyroxenite), and thus the specific numbers predicted here for χ_{PX}, depend on the melting law chosen (e.g., Pertermann and Hirschmann (2003) vs. Lambart et al. (2016)).

The general trends of model predictions in total melt volumes as a function of parameters are similar for groups A and B. For group C, the melting is generally more vigorous and virtually independent of C_{H2O_HP} and D_{HP}. According to group C, no connection between the subducted slab and intraplate volcanism is required. Melting is immediately caused by SSC (Ballmer et al., 2007; West et al., 2009; Ballmer et al., 2010), as soon as convective instability develops. Similarly, if much of the MTZ were hydrated (Bercovici and Karato, 2003; Nakagawa, 2017) and not just a layer above the stagnant slab, the locations of volcanism would be poorly related to those of the slab stagnation. However, according to the good spatial correlation between these two (Figure 1), we do not favor group C (or a homogenous distribution of hydrated material in the MTZ). In summary, group A can better explain the distribution (compared to group C) and geochemical signature (compared to group B) of pyroxenitic intraplate volcanism beneath continental lithosphere. However, we do not rule out that SSC alone can give rise to intraplate volcanism locally, e.g. due to regional enhancement of mafic materials (or other enriched lithologies) in the ambient mantle.

4. Discussion

According to our analysis, the timing of upwelling and magmatism, τ_u and τ_m, are mostly controlled by parameters that affect the local Rayleigh number, such as η_{eff} (or other rheological parameters not modeled here), and by parameters that affect the buoyancy of the hydrous material, such as C_{H2O_HP}. The amount of melting behaves generally consistently with τ_u and τ_m; early τ_u usually result in early τ_m and higher total melt volumes.

The parameter range, over which this robust behavior occurs, is realistic. 4000 wt.-ppm water in a 60 km thick hydrous layer are sufficient to promote intraplate volcanism soon after the slab arrives in the MTZ, e.g. in E China. Based on a few additional models (not shown), we find that there is a trade-off between critical water contents and layer thicknesses. At higher water contents (e.g. 6000 wt.-ppm) smaller layer thicknesses (~40 km) are required to obtain similar model behavior. Depending on the characteristics of the slab and the composition of the hydrated wedge, the total water flux transported to the transition zone may be sufficient to sustain these requirements, or even higher than that (Inoue et al., 1998). The water content in the MTZ has been estimated to be higher than 0.4 wt.-% (see section 4.4) (Pearson et al., 2014; Houser, 2016). Depending on the mechanisms of water delivery, the thickness of the hydrous layer above the slab may also be higher than the required 60 km, particularly if the whole MTZ is hydrated. Strong heterogeneity, such as a fracture zone with a large offset or a slab window, is not required to trigger early upwellings from the slab. An early onset on mantle melting requires effective viscosities ≤ 6.25×10^{18} Pa·s in the asthenosphere (see Fig. 7), consistent with independent estimates by Freed et al., (2006; 2017) and Bills et al., (2007). Even though poorly constrained (e.g., (Rudolph et al., 2015), relatively low viscosities on the order of 10^{19}~10^{20} Pa·s such as required for early upwelling may be realistic for the MTZ (Bills et al., 1994; James et al., 2000; Pollitz et al., 2001) at least for the hydrous layer and the hydrous upwellings. As we do not explicitly take into account the effects of water on reducing mantle viscosity (Fei et al., 2017), these constrained effective viscosities remain lower bounds. We expect that at a given η_{eff}, hydrous instability develops sooner and upwellings rise faster if water-dependent rheology were considered, even though the mostly dry matrix also has to be deformed. To get a rough idea how water dependent rheology would affect our results, several additional cases are tested. In these cases, the hydrous material (with water contents as in the reference case) is 20 times weaker than the ambient mantle. This weakening is only applied in the MTZ to keep results comparable to those of the reference case. Due to the imposed weakening, the onset of upwelling (τ_u) is advanced, but that of melting (τ_m) remains nearly unchanged. It takes ~10 Myr for hydrous materials to be conveyed from ~410 km depth to the base of the lithosphere regardless of τ_u. Nevertheless, the volume of melting is increased as more hydrous material goes unstable. Consequently, lower water contents and/or thinner hydrous layers (e.g. ~40 km) are required to obtain similar results as in the reference case without water-dependent rheology. Additional work is required to quantify the effects of hydrogen impurities on the viscosity of wadsleyite and ringwoodite for water contents that are significantly below saturation. In addition, the viscosity of the subducted slab may be depressed due to grain-size reduction during the crossing of the 410 km phase transition, and poor recovery afterwards (Riedel and Karato, 1997; Karato et al., 2001). Future modeling efforts are needed to explore the effects of a more realistic rheology on hydrous-upwelling dynamics and melting.

4.1 Distribution of volcanism in eastern Asia

Our model predictions of intraplate volcanism occurring directly above the stagnant slab is consistent with the distribution of intraplate volcanism in E Asia (Huang and Zheng, 2017; Yu et al., 2018) and globally (Figure 1). Specifically, our results imply that volcanism occurs in a belt between the slab tip and the hinge (i.e., where the slab first reaches the MTZ), or starts at a given distance from the hinge that is related to the timescale τ_m. In any case, large-scale poloidal (or toroidal) flow as imposed by slab sinking and roll-bock may pull upwellings towards the trench. In E China, the slab has been subducting and stagnating in the MTZ for more than 30 Myr and spreads ~3000 km away from the trench (Liu et al., 2017), and so does most of the observed intraplate volcanism (Liu et al., 2001; Ren et al., 2002).

Changbai volcano, located just over the hinge of the subducted slab (Zhao, 2004; Fukao and Obayashi, 2013; Liu et al., 2017), may be a special case. If we assume that it takes 10 Myr for the slab to sink through the upper mantle and reach the MTZ (Goes et al., 2011), Changbai volcano (Guo et al., 2016) may require a very early τ_m of < 5 Myr. As our model does not include the stage of the slab sinking trough the upper mantle, our τ_m are generally conservative estimates. Upwellings may indeed already start forming before the slab reaches the MTZ and begins to stagnate. In this case, the whole process may be advanced compared to our model predictions (or the constraint on η_{eff} relaxed). Alternatively, Kameyama & Nishioka (2012) propose that a strong local circulation near the hinge of the slab, above which Changbai volcano is located, is induced by the retreating and subduction of the Pacific slab. Tang et al. (2014) argue that a slab window (gap) in the subducted Pacific slab is located just beneath Changbai volcano. Note that in E Asia, the Pacific slab (and even earlier: the Izanagi slab) has been subducted for much more than 30 Myr and stagnated for at least 20 Myr (Liu et al., 2017). Hence, upwellings developing from that slab with $\tau_m < 20$ Myr are well sufficient to account for late Cenozoic volcanism in eastern China. Moreover, considering the heterogeneous nature of water distribution in the MTZ, our predicted τ_m should be upper bounds and melt volumes lower bounds.

The thickness and structure of the overlying lithosphere also controls the distribution of volcanism above the stagnant slab. For example, lithosphere farther away from the trench in central and western China is thicker than in the northeastern part, allowing less decompression melting and volcanism (Chen et al., 2008; Guo et al., 2018). This lithospheric structure of China may be an alternative explanation for the poor correlation between predictions in group C with observations. Sublithospheric structure may also control the distribution of volcanism through the geometry of SSC cells, (e.g., King and Anderson, 1995; King and Ritsema, 2000). In this case of "edge-driven convection", increased volcanism at a given distance from a step of lithospheric thickness would focus on the thin-lithosphere side. However, in China, volcanism commonly occurs on both sides of the step in lithospheric thickness, or both in- and outside of the basins (e.g. (Wang et al., 2006; Wang et al., 2017)).

4.2 Geochemical signatures of intraplate volcanism in NE China

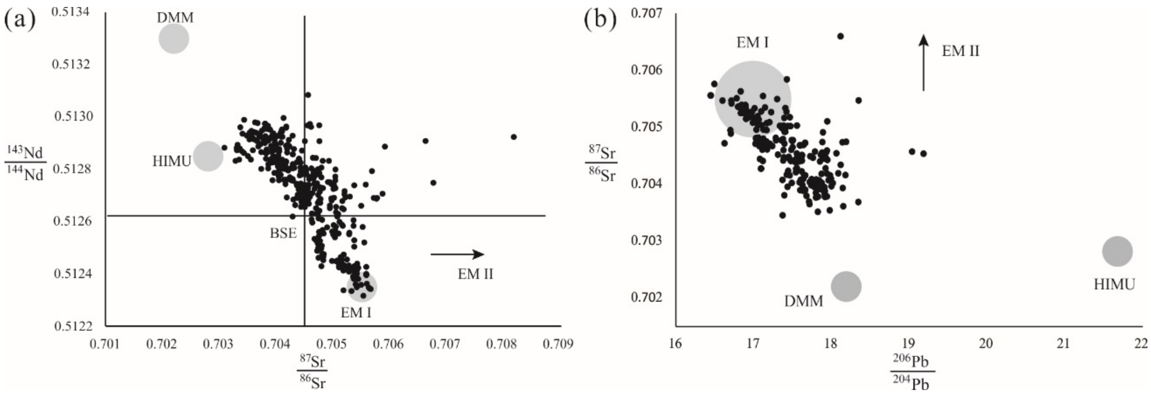

Figure 10: (a) $^{143}Nd/^{144}Nd$ vs $^{87}Sr/^{86}Sr$ and (b) $^{87}Sr/^{86}Sr$ vs $^{206}Pb/^{204}Pb$ of Cenozoic basalts in NE China showing the linear trend between two end-members. Data with higher Sr ratios are from the Bohai Bay Basin (Dong et al., 2010) and are consistent with sea-water alteration (Elderfield, 1986; Veizer, 1989). Data are from "GeoRoc" database (http://georoc.mpch-mainz.gwdg.de/georoc/; see Ext. Data Table). BSE is the assumed composition of the (primitive) Bulk Silicate Earth (McDonough and Sun, 1995). Isotopic ratios for mantle end-members are from Faure and Mensing (2005) except for the EMI end-member in (b), which is from Zindler and Hart (1986).

In order to compare our models to geochemical observations, we evaluate the isotopic record of intraplate volcanos in NE China, which have been interpreted in the context of the underlying stagnant slab (e.g., Zhao and Ohtani (2009) (Figure 10). The data can largely be explained by a mixture of two geochemical end-members, which are similar to DMM (or between HIMU and DMM), i.e. similar to the source of "enriched" Indian-style MORB) and EM1. Thus, a reasonable interpretation is that two mantle components contribute to mantle melting in the example study area. This two-components interpretation is consistent with previous studies of Cenozoic basalts in North and northeastern China (Zhang et al., 1995; Yan and Zhao, 2008; Zeng et al., 2011; Kuritani et al., 2013; Liu et al., 2015; Li et al., 2016; Chen et al., 2017). Although some authors have argued for a third component on the basis of Pb isotopes (Kuritani et al., 2011), this component is related to ancient – instead of recent – hydration of the MTZ, and would be indistinguishable from the hydrous material in our thermo-mechanical model. While the origin of mantle end-members remains controversial, we consider that the apparent DMM-HIMU-like end-member (Figure 10), is volatile-rich peridotite, e.g. related to fluid-mediated metasomatism

(Keppler, 1996; Kogiso et al., 1997; Castro and Gerya, 2008) and the EM1 component is related to pyroxenite that may be formed in the mantle wedge due to melting of silicic sediments (Bodinier and Godard, 2003; Castro and Gerya, 2008; Prelević et al., 2008). These are assumed to be the two magmatic components (hydrous peridotite and pyroxenite) in our model.

Our models and conclusions, however, are not dependent on this specific interpretation. Our conclusions remain robust as long as two components with geochemical signatures similar to EM1 and DMM-HIMU are located in the hydrous layer. Moreover, we require that the melting behavior of the lithological components that carry the EM1 and DMM-HIMU end-members as evident in NE China volcanism are adequately described by that of pyroxenite, and volatile-rich peridotite, respectively. In which proportions they would have to be present in the MTZ depends on their relevant melting temperatures (and thus specific major-element compositions). In other words, these proportions would shift as different melting laws (e.g., McKenzie and Bickle, 1990) than used here (Katz et al., 2003; Pertermann and Hirschmann, 2003) were considered (see Figure 3a).

Figure 10 does neither display a dominant contribution of HIMU nor of EM1. Accordingly, we estimate that the relative contributions of pyroxenite and HP to magmatism should be similar to each other. This constraint limits the range of initial pyroxenite fractions in the hydrous layer to about 1.2%~2.3% given our melting laws (Figure 8). Due to the high melt productivity of pyroxenite in the melting model applied (Figure 3a), these initial pyroxenite fractions in the hydrous layer are lower bounds.

4.3 Intraplate volcanism in central Europe, western United States, and NE Australia

Intraplate volcanism across the Cenozoic Central European Volcanic Province (CEVP) and Cenozoic intraplate volcanism in the western US (www.navdat.org) also remain poorly understood. In our opinion, intraplate volcanism in central Europe and the western US may be associated with hydrous upwellings from the underlying stagnant slab, similar to the situation in NE China. As these two areas are underlain by a stagnant slab in the MTZ (Piromallo and Morelli, 2003; Faccenna and Becker, 2010; Schmandt and Lin, 2014), any associated hydrous materials in the MTZ are expected to trigger self-buoyant upwellings and sustain volcanism. Focused vertical upwellings are imaged by high-resolution seismic tomography, and are proposed to account for intraplate magmatism in the western US (Sigloch et al., 2008; West et al., 2009) and central Europe (Ritter et al., 2001). In particular, intraplate volcanism in central Europe predominantly occurs above the edge of the slab that stagnates in the MTZ (Faccenna et al., 2010), i.e. where our models predict the first upwellings to occur.

Intraplate magmatism is low in volume but widespread across Europe from the early Tertiary to present (Wilson and Downes, 2006), characterized by oceanic island basalt (OIB) geochemical signatures with a significant contribution of the HIMU end-member (Jung and Masberg, 1998; Wedepohl and Baumann, 1999; Lustrino and Wilson, 2007; Faccenna et al., 2010). Mantle upwelling and continental rifting in this area has been proposed to be related to return flow due to plate subduction and slab detachment during the Alpine collision (Merle and Michon, 2001; Wilson and Downes, 2005; Faccenna et al., 2010). However, as mentioned above, subducted slabs are expected to primarily induce horizontal toroidal flow (Billen and Gurnis, 2001; Long and Silver, 2008; Liu and Stegman, 2011; Chen et al., 2016). We identify hydrous upwellings from the edge of the underlying stagnant slab as a viable alternative hypothesis.

Magmatism in western US is widely distributed and large in volume compared to the CEVP. This magmatism includes the Columbia River Basalts province and the Yellowstone-Snake River Plain hotspot track, which have been related to focused mantle upwelling through a slab window (Madsen et al., 2006; Liu and Stegman, 2012) or a deep-seated plume (Morgan, 1972; Pierce et al., 1992; Takahahshi et al., 1998; Hooper et al., 2002; Camp et al., 2003; Nelson and Grand, 2018). However, several volcanic fields in the western US remain poorly understood. For example, intraplate alkalic volcanism in Leucite Hills has been attributed to fluid-mediated metasomatism of the upper mantle (Vollmer et al., 1984) or mantle upwellings facilitated by slab tearing (Dudás, 1991; Duke et al., 2014). In addition, western US intraplate volcanos have also been attributed to continental extension and rifting (e.g., Christiansen and Lipman, 1972; Fitton et al., 1991; Lipman and Glazner, 1991; Cosca et al., 2014), shear-driven upwelling (Conrad et al., 2011) or edge-driven convection (Ballmer et al., 2015; Rudzitis et al., 2016). We suggest that the process proposed in our model may be an alternative explanation. Models are not mutually exclusive; for instance, hydrated upwellings could be focused along the edges of the slab to generate the lineation found by Duke et al. (2014), or be entrained by SSC/edge-driven flow to sustain melting along the edges of the Colorado Plateau (Afonso et al., 2016).

Finally, magmatic activity in Australia may also be (at least partially) related to an underlying slab. The NE corner of the Australian continent, with abundant Cenozoic intraplate volcanism ((Wellman and McDougall, 1974); Figure 1), is underlain by (the edge of) a fossil slab (Hall and Spakman, 2002). Volcanism due to hydrous upwellings from the fossil slab (edge) cannot be ruled out by geochemical observations (Zhang et al., 2001). While alternative mechanisms have been proposed (e.g., (Davies et al., 2015), our models imply that hydrous upwellings can support sublithospheric melting over long timescales (Motoki and Ballmer, 2015), and thus may be relevant even above fossil slabs in the MTZ.

We note that direct comparison between the predictions of our simplified models and the exact locations, volumes and chemistry of intraplate volcanism remains challenging. First, the ratio of intrusive and extrusive magmatism, and the interaction of ascending magmas with the continental crust is poorly constrained. Second, our 2D models do not account for trench-perpendicular flow and sublithospheric topography, which would both affect the patterns of conveyance and lead to different patterns of volcanism. Indeed, there is a long and complex history of subduction, particularly in the western US (Bunge and Grand, 2000) and Europe (Faccenna et al., 2001). Nevertheless, comparison on a first-order level (see sections 4.1-4.3), also in terms of the global distribution of continental intraplate volcanism (Fig. 1), lends credibility to the importance of hydrous upwellings from the subducted slab.

4.4 Water in the mantle

The water storage capacity of the mantle is suggested to be on the order of three, or even up to ten, ocean masses (Ringwood, 1975; Ahrens, 1989; Ohtani, 2005; Cowan and Abbot, 2014). An important reservoir involves the MTZ, which can host up to 3 wt.-%, or ~30,000 wt.-ppm, H_2O (Ohtani et al., 1995; Kohlstedt et al., 1996; Bolfan-Casanova et al., 2000; Murakami et al., 2002; Ohtani et al., 2004). Based on diamond inclusions, Pearson et al. (2014) found direct evidence that the water content in at least some regions of the MTZ is ~1 wt.-%, or ~10,000 wt.-ppm. However, seismic constraints indicate that the average water content over vast regions of the MTZ may be quite a bit lower than saturation, i.e. 1000~5000 wt.-ppm (Angel et al., 2001; Huang et al., 2005; Wang et al., 2006; Houser, 2016; Matsuno et al., 2017). According to our predictions, instability of hydrous material that is sufficiently swift to support sublithospheric magmatism just requires ~4000 wt.-ppm H_2O in a 60-km thick layer.

While our model predictions are largely independent of the specific origin of the water, it remains an important question. As the mantle is steadily outgassing water due to volcanism, there has to be significant supplement of water of a similar order. Considering that water can most efficiently be transported from the surface and through the upper mantle along cool geotherms (Frost, 2006; Komabayashi, 2006; Nishi et al., 2014; Ohira et al., 2014), subduction of hydrous sediments and the hydrated slab itself is perhaps the best candidate for water delivery to the MTZ (e.g. (Inoue et al., 1995; Ohtani et al., 2004; Faccenda et al., 2009; van Keken et al., 2011)). At least an old and fast subducting plate (such as in E Asia) is able to transport water to the MTZ efficiently (Iwamori, 2004). While significant dehydration occurs at shallow depths (Jarrard, 2003), nominally anhydrous minerals in the oceanic crust and the overlying mantle wedge can carry significant amounts of water across the "choke point", i.e. across the water solubility trough at 6 GPa (Frost, 2006; Komabayashi, 2006; Iwamori, 2007; Nishi et al., 2014; Ohira et al., 2014). Alternatively, water may be transported in the core of the slab (serpentinized lithosphere; (Faccenda et al., 2008)), from which it would be slowly released in the MTZ. Accordingly, the hydrous-peridotite layer in our model would not necessarily be directly related to the recently subducted slab; instead, hydrous material may have progressively accumulated in the MTZ, thus being related to variably ancient subduction (Hofmann, 1997; Kuritani et al., 2011).

Continuous upwellings of hydrous materials may account for the geophysically constrained relatively low water content in the MTZ (Huang et al., 2005; Houser, 2016). Subducted slabs have transported water from the surface to the MTZ over very long timescales, at least since the onset of modern-style plate tectonics at ~2 Ga (Davies, 1992;

Smithies et al., 2003). Accordingly, it appears difficult to explain that the MTZ is still far away from saturation. Our forward models offer a simple explanation. Whenever there is a sufficiently thick hydrous layer in the MTZ (i.e., even without the presence of a stagnant slab), upwellings instabilities should soon develop and rise at least to 410 km depth. In other words, hydrated (>3000 ppm water) layers >60 km thick are not expected to survive for geological timescales, corresponding to a total mass of ~0.1 oceans in the MTZ, i.e. well below previous estimates (Ringwood, 1975; Ahrens, 1989; Ohtani, 2005; Cowan and Abbot, 2014; Grayver et al., 2017)). Related mantle melting should occur wherever significant hydrous material has accumulated in the MTZ, and is entrained by SSC. While SSC should be well-developed beneath the old continents, the onset of SSC may take up to ~70 Myr beneath oceanic lithosphere (Solomatov and Moresi, 2000; Ballmer et al., 2009). A potential example of oceanic volcanism that is related to recycling of a volatile-rich reservoir in the MTZ involves the Bermuda Islands (Mazza et al., 2019).

As the hydrous plumes cross the phase transition at 410 km depth, most of the water may be left behind in the MTZ due to the small water capacity in the upper mantle, e.g. due to the "transition-zone water filter" effect described by Bercovici and Karato (2003). As a crude simplification, we assume that any water exceeding a threshold of 400 ppm simply disappears from the system (i.e., the convecting solid matrix) by stabilizing a gravitationally-stable volatile-rich melt layer just above 410 km depth. This assumption may lead to an underestimation of the volume of the hydrous materials that ascend into the upper mantle, because the stabilization of such a layer should lead to a redistribution of volatiles, and widespread saturation of mantle rocks just beneath the 410 discontinuity. Evidence for the stabilization of a melt layer comes from seismic observations (Revenaugh and Sipkin, 1994; Song et al., 2004; Jasbinsek and Dueker, 2007; Tauzin et al., 2010). As this layer would be gravitationally-stable (Ohtani et al., 1995; Ohtani and Maeda, 2001) and should only extend laterally, it will not significantly affect the driving forces of the mantle upwellings. The melt layer has been invoked to have important implications for the geochemical evolution of mantle reservoirs, partially separating the upper-mantle reservoir from the rest of the mantle like a "filter" (Bercovici and Karato, 2003). Future studies should take into account the explicit effects of the presence of such a melt layer on the distribution of hydrous rocks in the MTZ explicitly. Lateral re-distribution of volatiles through the melt layer may lead to widespread H_2O-saturation in the uppermost MTZ due to buoyancy-driven mantle flow. For example, downwellings may be hydrated as they dive into the MTZ, potentially diminishing the vigor of upwellings (Leahy and Bercovici, 2007). Along these lines, hydrous upwellings, at least partially bypassing the “transition-zone water filter”, may play an important role for material transport, and mantle evolution.

5. Conclusion

(1) Upwellings rise from the buoyant hydrous layer atop a stagnant slab within a few Myr after the slab arrives in the MTZ. They rise to ~410 km depth, where they intermittently stall, and are ultimately entrained by sublithospheric small-scale convection (SSC).

(2) Partial melting takes place at the base of the lithosphere after the arrival of hydrous materials that are conveyed by SSC cells.

(3) >0.3 wt.-% water in a 60 km thick hydrous layer atop the slab, or slightly less as water-dependent rheology is considered, is required to produce early upwelling of hydrated material and early melting beneath the lithosphere in order to account for patterns of volcanism in e.g. NE China. Relatively low asthenospheric viscosities of smaller than $\sim 7 \cdot 10^{18}$ Pa·s are also needed. Higher water contents, a thicker hydrous layer, as well as lower viscosities tend to advance and boost melting.

(4) An initial condition with moderate amounts of hydrous materials as well as small amounts (~2%) of mafic material in a layer above the slab can account for the geochemical observations in northeastern China, as well as the spatial association of volcanism to the underlying stagnant slab.

(5) Intraplate continental volcanism above the stagnant slab can be explained by the interaction of (bottom-up) self-buoyant instability of hydrous material and top-down driven SSC.

Acknowledgements

We wish to thank Kosuke Ueda, Lara Kalnins and Sebastien Pilet for significant comments and suggestions during earlier stages of this work. We also thank M. Kameyama, G. Richard and two anonymous reviewers for their helpful comments, and T. Becker for thoughtful editorial handling. This work has been supported by the China Scholarship Council, Natural Science Foundation of China (Grant Nos. 41776057, 91858213) and the Swiss National Science Foundation (Grant No. 200021_165682/1). The version of Citcom that has been used here, along with the relevant input files, is available upon request.

6. References

Afonso, J. C., Zlotnik, S., & Fernàndez, M. (2008), Effects of compositional and rheological stratifications on small-scale convection under the oceans: Implications for the thickness of oceanic lithosphere and seafloor flattening, *Geophysical Research Letters*, *35*(20).

Afonso, J. C., Rawlinson, N., Yang, Y., Schutt, D. L., Jones, A. G., Fullea, J., & Griffin, W. L. (2016), 3‐D multiobservable probabilistic inversion for the compositional and thermal structure of the lithosphere and upper mantle: III. Thermochemical tomography in the Western‐Central US, *Journal of Geophysical Research: Solid Earth*, *121*(10), 7337-7370.

Ahrens, T. J. (1989), Water storage in the mantle, *Nature*, *342*(6246), 122-123.

Andrault, D., et al. (2018), Deep and persistent melt layer in the Archaean mantle, *Nature Geoscience*, *11*(2), 139-143.

Angel, R., Frost, D., Ross, N., & Hemley, R. (2001), Stabilities and equations of state of dense hydrous magnesium silicates, *Physics of the Earth and Planetary Interiors*, *127*(1-4), 181-196.

Aoki, I., & Takahashi, E. (2004), Density of MORB eclogite in the upper mantle, *Physics of the Earth and Planetary Interiors*, *143-144*, 129-143.

Balbas, A., Koppers, A. A. P., Kent, D. V., Konrad, K., & Clark, P. U. (2016), Identification of the short-lived Santa Rosa geomagnetic excursion in lavas on Floreana Island (Galapagos) by40Ar/39Ar geochronology, *Geology*, *44*(5), 359-362.

Ballmer, M. D., van Keken, P. E., & Ito, G. (2015a), Hotspots, Large Igneous Provinces, and Melting Anomalies, 393-459.

Ballmer, M. D., Ito, G., van Hunen, J., & Tackley, P. J. (2010), Small-scale sublithospheric convection reconciles geochemistry and geochronology of 'Superplume' volcanism in the western and south Pacific, *Earth and Planetary Science Letters*, *290*(1-2), 224-232.

Ballmer, M. D., Conrad, C. P., Smith, E. I., & Harmon, N. (2013), Non-hotspot volcano chains produced by migration of shear-driven upwelling toward the East Pacific Rise, *Geology*, *41*(4), 479-482.

Ballmer, M. D., Conrad, C. P., Smith, E. I., & Johnsen, R. (2015), Intraplate volcanism at the edges of the Colorado Plateau sustained by a combination of triggered edge-driven convection and shear-driven upwelling, *Geochemistry, Geophysics, Geosystems*, *16*(2), 366-379.

Ballmer, M. D., Schmerr, N. C., Nakagawa, T., & Ritsema, J. (2015), Compositional mantle layering revealed by slab stagnation at~ 1000-km depth, *Science advances*, *1*(11), e1500815.

Ballmer, M. D., van Hunen, J., Ito, G., Tackley, P. J., & Bianco, T. A. (2007), Non-hotspot volcano chains originating from small-scale sublithospheric convection, *Geophysical Research Letters*, *34*(23).

Ballmer, M. D., van Hunen, J., Ito, G., Bianco, T. A., & Tackley, P. J. (2009), Intraplate volcanism with complex age-distance patterns: A case for small-scale sublithospheric convection, *Geochemistry, Geophysics, Geosystems*, *10*(6).

Ballmer, M. D., Schumacher, L., Lekic, V., Thomas, C., & Ito, G. (2016), Compositional layering within the large low shear-wave velocity provinces in the lower mantle, *Geochemistry, Geophysics, Geosystems*, *17*(12), 5056-5077.

Batiza, R. (1980), Origin and petrology of young oceanic central volcanoes: Are most tholeiitic rather than alkalic?, *Geology*, *8*(10), 477-482.

Batiza, R. (1982), Abundances, distribution and sizes of volcanoes in the Pacific Ocean and implications for the origin of non-hotspot volcanoes, *Earth and Planetary Science Letters*, *60*(2), 195-206.

Bercovici, D., & Karato, S.-i. (2003), Whole-mantle convection and the transition-zone water filter, *Nature*, *425*(6953), 39-44.

Bianco, T. A., Ito, G., van Hunen, J., Ballmer, M. D., & Mahoney, J. J. (2011), Geochemical variations at intraplate hot spots caused by variable melting of a veined mantle plume, *Geochemistry, Geophysics, Geosystems*, *12*(7), n/a-n/a.

Billen, M. I., & Gurnis, M. (2001), A low viscosity wedge in subduction zones, *Earth and Planetary Science Letters*, *193*(1), 227-236.

Bills, B. G., Currey, D. R., & Marshall, G. A. (1994), Viscosity estimates for the crust and upper mantle from patterns of lacustrine shoreline deformation in the Eastern Great Basin, *Journal of Geophysical Research: Solid Earth*, *99*(B11), 22059-22086.

Bills, B. G., Adams, K. D., & Wesnousky, S. G. (2007), Viscosity structure of the crust and upper mantle in western Nevada from isostatic rebound patterns of the late Pleistocene Lake Lahontan high shoreline, *Journal of Geophysical Research*, *112*(B6).

Bodinier, J.-L., & Godard, M. (2003), Orogenic, ophiolitic, and abyssal peridotites, *Treatise on geochemistry*, *2*, 568.

Bolfan-Casanova, N., Keppler, H., & Rubie, D. C. (2000), Water partitioning between nominally anhydrous minerals in the MgO–SiO2–H2O system up to 24 GPa: implications for the distribution of water in the Earth's mantle, *Earth and Planetary Science Letters*, *182*(3-4), 209-221.

Brandenburg, J. P., & Keken, P. E. V. (2007), Deep storage of oceanic crust in a vigorously convecting mantle, *Journal of Geophysical Research Solid Earth*, *112*(B6), -.

Bunge, H.-P., & Grand, S. P. (2000), Mesozoic plate-motion history below the northeast Pacific Ocean from seismic images of the subducted Farallon slab, *Nature*, *405*(6784), 337.

Burke, K., Steinberger, B., Torsvik, T. H., & Smethurst, M. A. (2008), Plume Generation Zones at the margins of Large Low Shear Velocity Provinces on the core–mantle boundary, *Earth and Planetary Science Letters*, *265*(1-2), 49-60.

Camp, V. E., Ross, M. E., & Hanson, W. E. (2003), Genesis of flood basalts and Basin and Range volcanic rocks from Steens Mountain to the Malheur River Gorge, Oregon, *Geological Society of America Bulletin*, *115*(1), 105-128.

Cao, L., Wang, Z., Wu, S., & Gao, X. (2014), A new model of slab tear of the subducting Philippine Sea Plate associated with Kyushu–Palau Ridge subduction, *Tectonophysics*, *636*, 158-169.

Castro, A., & Gerya, T. V. (2008), Magmatic implications of mantle wedge plumes: Experimental study, *Lithos*, *103*(1-2), 138-148.

Chen, H., Xia, Q.-K., Ingrin, J., Deloule, E., & Yao, B. (2017), Heterogeneous source components of intraplate basalts from NE China induced by the ongoing Pacific slab subduction, *Earth and Planetary Science Letters*, *459*, 208-220.

Chen, L., Tao, W., Zhao, L., & Zheng, T. (2008), Distinct lateral variation of lithospheric thickness in the Northeastern North China Craton, *Earth and Planetary Science Letters*, *267*(1-2), 56-68.

Chen, Z., Schellart, W. P., Strak, V., & Duarte, J. C. (2016), Does subduction-induced mantle flow drive backarc extension?, *Earth and Planetary Science Letters*, *441*, 200-210.

Christensen, U. (1984), Convection with pressure-and temperature-dependent non-Newtonian rheology, *Geophysical Journal International*, *77*(2), 343-384.

Christiansen, R., & Lipman, P. W. (1972), A Discussion on volcanism and the structure of the Earth-Cenozoic volcanism and plate-tectonic evolution of the Western United States. II. Late cenozoic, *Phil. Trans. R. Soc. Lond. A*, *271*(1213), 249-284.

Clouard, V., & Bonneville, A. (2005), Ages of seamounts, islands, and plateaus on the Pacific plate, *Geological Society of America Special Papers*, *388*, 71-90.

Conrad, C. P., Bianco, T. A., Smith, E. I., & Wessel, P. (2011), Patterns of intraplate volcanism controlled by asthenospheric shear, *Nature Geoscience*, *4*(5), 317-321.

Conrad, C. P., Wu, B., Smith, E. I., Bianco, T. A., & Tibbetts, A. (2010), Shear-driven upwelling induced by lateral viscosity variations and asthenospheric shear: A mechanism for intraplate volcanism, *Physics of the Earth and Planetary Interiors*, *178*(3-4), 162-175.

Cosca, M. A., Thompson, R. A., Lee, J. P., Turner, K. J., Neymark, L. A., & Premo, W. R. (2014), 40Ar/39Ar geochronology, isotope geochemistry (Sr, Nd, Pb), and petrology of alkaline lavas near Yampa, Colorado: Migration of alkaline volcanism and evolution of the northern Rio Grande rift, *Geosphere*, *10*(2), 374-400.

Courtillot, V., Davaille, A., Besse, J., & Stock, J. (2003), Three distinct types of hotspots in the Earth's mantle, *Earth and Planetary Science Letters*, *205*(3-4), 295-308.

Cowan, N. B., & Abbot, D. S. (2014), Water cycling between ocean and mantle: Super-Earths need not be waterworlds, *The Astrophysical Journal*, *781*(1), 27.

Davies, D., Rawlinson, N., Iaffaldano, G., & Campbell, I. (2015), Lithospheric controls on magma composition along Earth's longest continental hotspot track, *Nature*, *525*(7570), 511.

Davies, G. F. (1992), On the emergence of plate tectonics, *Geology*, *20*(11), 963-966.

Demidjuk, Z., Turner, S., Sandiford, M., George, R., Foden, J., & Etheridge, M. (2007), U-series isotope and geodynamic constraints on mantle melting processes beneath the Newer Volcanic Province in South Australia, *Earth and Planetary Science Letters*, *261*(3-4), 517-533.

Dickinson, W. R., & Snyder, W. S. (1979), Geometry of Subducted Slabs Related to San Andreas Transform, *The Journal of Geology*, *87*(6), 609-627.

Dong, Y., Xiao, L., Zhou, H., Du, J., Zhang, N., Xiang, H., Wang, C., Zhao, Z., & Huang, H. (2010), Volcanism of the Nanpu Sag in the Bohai Bay Basin, Eastern China: Geochemistry, petrogenesis, and implications for tectonic setting, *Journal of Asian Earth Sciences*, *39*(3), 173-191.

Dudás, F. Ö. (1991), Geochemistry of igneous rocks from the Crazy Mountains, Montana, and tectonic models for the Montana Alkalic Province, *Journal of Geophysical Research: Solid Earth*, *96*(B8), 13261-13277.

Duke, G. I., Carlson, R. W., Frost, C. D., Hearn, B. C., & Eby, G. N. (2014), Continent-scale linearity of kimberlite–carbonatite magmatism, mid-continent North America, *Earth and Planetary Science Letters*, *403*, 1-14.

Dumoulin, C., Choblet, G., & Doin, M. P. (2008), Convective interactions between oceanic lithosphere and asthenosphere: Influence of a transform fault, *Earth and Planetary Science Letters*, *274*(3-4), 301-309.

Dumoulin, C., Doin, M.-P., Arcay, D., & Fleitout, L. (2004), Onset of small-scale instabilities at the base of the lithosphere: scaling laws and role of pre-existing lithospheric structures, *Geophysical Journal International*, *160*(1), 345-357.

Elderfield, H. (1986), Strontium isotope stratigraphy, *Palaeogeography, palaeoclimatology, palaeoecology*, *57*(1), 71-90.

Elkins-Tanton, L. T. (2007), Continental magmatism, volatile recycling, and a heterogeneous mantle caused by lithospheric gravitational instabilities, *Journal of Geophysical Research*, *112*(B3).

Elliott, T. (1997), Fractionation of U and Th during mantle melting: a reprise, *Chemical Geology*, *139*(1-4), 165-183.

Faccenda, M., Gerya, T. V., & Burlini, L. (2009), Deep slab hydration induced by bending-related variations in tectonic pressure, *Nature Geoscience*, *2*(11), 790-793.

Faccenda, M., Burlini, L., Gerya, T. V., & Mainprice, D. (2008), Fault-induced seismic anisotropy by hydration in subducting oceanic plates, *Nature*, *455*(7216), 1097-1100.

Faccenna, C., & Becker, T. W. (2010), Shaping mobile belts by small-scale convection, *Nature*, *465*(7298), 602-605.

Faccenna, C., Rossetti, F., Becker, T. W., Lucente, F. P., & Jolivet, L. (2001), History of subduction and back arc extension in the Central Mediterranean, *Geophysical Journal International*, *145*(3), 809-820.

Faccenna, C., Becker, T. W., Lallemand, S., Lagabrielle, Y., Funiciello, F., & Piromallo, C. (2010), Subduction-triggered magmatic pulses: A new class of plumes?, *Earth and Planetary Science Letters*, *299*(1-2), 54-68.

Faure, G., & Mensing, T. M. (2005), *Isotopes: principles and applications*, Wiley-Blackwell.

Fei, H., Yamazaki, D., Sakurai, M., Miyajima, N., Ohfuji, H., Katsura, T., & Yamamoto, T. (2017), A nearly water-saturated mantle transition zone inferred from mineral viscosity, *Science advances*, *3*(6), e1603024.

Férot, A., & Bolfan-Casanova, N. (2012), Water storage capacity in olivine and pyroxene to 14GPa: Implications for the water content of the Earth's upper mantle and nature of seismic discontinuities, *Earth and Planetary Science Letters*, *349-350*, 218-230.

Fitton, J. G., James, D., & Leeman, W. P. (1991), Basic magmatism associated with Late Cenozoic extension in the western United States: Compositional variations in space and time, *Journal of Geophysical Research: Solid Earth*, *96*(B8), 13693-13711.

Freed, A. M., Bürgmann, R., Calais, E., Freymueller, J., & Hreinsdóttir, S. (2006), Implications of deformation following the 2002 Denali, Alaska, earthquake for postseismic relaxation processes and lithospheric rheology, *Journal of Geophysical Research*, *111*(B1).

Freed, A. M., Hashima, A., Becker, T. W., Okaya, D. A., Sato, H., & Hatanaka, Y. (2017), Resolving depth-dependent subduction zone viscosity and afterslip from postseismic displacements following the 2011 Tohoku-oki, Japan earthquake, *Earth and Planetary Science Letters*, *459*, 279-290.

Frost, D. J. (2006), The stability of hydrous mantle phases, *Reviews in Mineralogy and Geochemistry*, *62*(1), 243-271.

Fukao, Y., & Obayashi, M. (2013), Subducted slabs stagnant above, penetrating through, and trapped below the 660 km discontinuity, *Journal of Geophysical Research: Solid Earth*, *118*(11), 5920-5938.

Fukao, Y., Widiyantoro, S., & Obayashi, M. (2001), Stagnant slabs in the upper and lower mantle transition region, *Reviews of Geophysics*, *39*(3), 291-323.

Garcia, M. O., Swinnard, L., Weis, D., Greene, A. R., Tagami, T., Sano, H., & Gandy, C. E. (2010), Petrology, Geochemistry and Geochronology of Kaua'i Lavas over 4·5 Myr: Implications for the Origin of Rejuvenated Volcanism and the Evolution of the Hawaiian Plume, *Journal of Petrology*, *51*(7), 1507-1540.

Gerbault, M., Burov, E. B., Poliakov, A. N. B., & Daignières, M. (1999), Do faults trigger folding in the lithosphere?, *Geophysical Research Letters*, *26*(2), 271-274.

Gerya, T. V., Yuen, D. A., & Sevre, E. O. D. (2004), Dynamical causes for incipient magma chambers above slabs, *Geology*, *32*(1), 89.

Goes, S., Capitanio, F. A., Morra, G., Seton, M., & Giardini, D. (2011), Signatures of downgoing plate-buoyancy driven subduction in Cenozoic plate motions, *Physics of the Earth and Planetary Interiors*, *184*(1-2), 1-13.

Grayver, A. V., Kuvshinov, A. V., Khan, A., Munch, F. D., Sabaka, T. J., & Toffnerclausen, L. (2017), Joint Inversion of Satellite-Detected Tidal and Magnetospheric Signals Constrains Electrical Conductivity and Water Content of the Upper Mantle and Transition Zone, *Geophysical Research Letters*, *44*(12).

Guo, Z., Chen, Y. J., Ning, J., Yang, Y., Afonso, J. C., & Tang, Y. (2016), Seismic evidence of on-going sublithosphere upper mantle convection for intra-plate volcanism in Northeast China, *Earth and Planetary Science Letters*, *433*, 31-43.

Guo, Z., Wang, K., Yang, Y., Tang, Y., Chen, Y. J., & Hung, S. H. (2018), The origin and mantle dynamics of quaternary intraplate volcanism in Northeast China from joint inversion of surface wave and body wave, *Journal of Geophysical Research: Solid Earth*, *123*(3), 2410-2425.

Hall, R., & Spakman, W. (2002), Subducted slabs beneath the eastern Indonesia–Tonga region: insights from tomography, *Earth and Planetary Science Letters*, *201*(2), 321-336.

Hanyu, T., & Kaneoka, I. (1997), The uniform and low 3 He/4 He ratios of HIMU basalts as evidence for their origin as recycled materials, *Nature*, *390*(6657), 273.

Hernlund, J. W., Tackley, P. J., & Stevenson, D. J. (2008), Buoyant melting instabilities beneath extending lithosphere: 1. Numerical models, *Journal of Geophysical Research*, *113*(B4).

Hieronymus, C. F., & Bercovici, D. (2000), Non-hotspot formation of volcanic chains: Control of tectonic and flexural stresses on magma transport, *Earth and Planetary Science Letters*, *181*(4), 539-554.

Hirose, K., Fei, Y., Ma, Y., & Mao, H.-K. (1999), The fate of subducted basaltic crust in the Earth's lower mantle, *Nature*, *397*(6714), 53.

Hirschmann, M. M., & Stolper, E. M. (1996), A possible role for garnet pyroxenite in the origin of the "garnet signature" in MORB, *Contributions To Mineralogy and Petrology*, *124*(2), 185-208.

Hofmann, A. (1997), Mantle geochemistry: the message from oceanic volcanism, *Nature*, *385*(6613), 219.

Holtzman, B. K., Groebner, N. J., Zimmerman, M. E., Ginsberg, S. B., & Kohlstedt, D. L. (2003), Stress-driven melt segregation in partially molten rocks, *Geochemistry, Geophysics, Geosystems*, *4*(5).

Hooper, P., Binger, G., & Lees, K. (2002), Ages of the Steens and Columbia River flood basalts and their relationship to extension-related calc-alkalic volcanism in eastern Oregon, *Geological Society of America Bulletin*, *114*(1), 43-50.

Houser, C. (2016), Global seismic data reveal little water in the mantle transition zone, *Earth and Planetary Science Letters*, *448*, 94-101.

Huang, J. (2003), Controls on sublithospheric small-scale convection, *Journal of Geophysical Research*, *108*(B8).

Huang, J., Zhong, S., & van Hunen, J. (2003), Controls on sublithospheric small-scale convection, *Journal of Geophysical Research*, *108*(B8).

Huang, S., & Zheng, Y. (2017), Mantle geochemistry: Insights from ocean island basalts, *Science China Earth Sciences*, *60*(11), 1976-2000.

Huang, X., Xu, Y., & Karato, S.-i. (2005), Water content in the transition zone from electrical conductivity of wadsleyite and ringwoodite, *Nature*, *434*(7034), 746.

Inoue, T., Yurimoto, H., & Kudoh, Y. (1995), Hydrous modified spinel, Mg1. 75SiH0. 5O4: a new water reservoir in the mantle transition region, *Geophysical Research Letters*, *22*(2), 117-120.

Inoue, T., Weidner, D. J., Northrup, P. A., & Parise, J. B. (1998), Elastic properties of hydrous ringwoodite (γ-phase) in Mg2SiO4, *Earth and Planetary Science Letters*, *160*(1-2), 107-113.

Inoue, T., Tanimoto, Y., Irifune, T., Suzuki, T., Fukui, H., & Ohtaka, O. (2004), Thermal expansion of wadsleyite, ringwoodite, hydrous wadsleyite and hydrous ringwoodite, *Physics of the Earth and Planetary Interiors*, *143-144*, 279-290.

Ito, E., & Takahashi, E. (1989), Postspinel transformations in the system Mg2SiO4-Fe2SiO4and some geophysical implications, *Journal of Geophysical Research: Solid Earth*, *94*(B8), 10637-10646.

Iwamori, H. (2004), Phase relations of peridotites under H2O-saturated conditions and ability of subducting plates for transportation of H2O, *Earth and Planetary Science Letters*, *227*(1-2), 57-71.

Iwamori, H. (2007), Transportation of H2O beneath the Japan arcs and its implications for global water circulation, *Chemical Geology*, *239*(3-4), 182-198.

Jacobsen, S. D., Smyth, J. R., Spetzler, H., Holl, C. M., & Frost, D. J. (2004), Sound velocities and elastic constants of iron-bearing hydrous ringwoodite, *Physics of the Earth and Planetary Interiors*, *143-144*, 47-56.

James, T. S., Clague, J. J., Wang, K., & Hutchinson, I. (2000), Postglacial rebound at the northern Cascadia subduction zone, *Quaternary Science Reviews*, *19*(14-15), 1527-1541.

Jarrard, R. D. (2003), Subduction fluxes of water, carbon dioxide, chlorine, and potassium, *Geochemistry, Geophysics, Geosystems*, *4*(5), n/a-n/a.

Jasbinsek, J., & Dueker, K. (2007), Ubiquitous low-velocity layer atop the 410-km discontinuity in the northern Rocky Mountains, *Geochemistry, Geophysics, Geosystems*, *8*(10), n/a-n/a.

Jung, S., & Masberg, P. (1998), Major-and trace-element systematics and isotope geochemistry of Cenozoic mafic volcanic rocks from the Vogelsberg (central Germany): constraints on the origin of continental alkaline and tholeiitic basalts and their mantle sources, *Journal of Volcanology and Geothermal Research*, *86*(1), 151-177.

Kaislaniemi, L., & van Hunen, J. (2014), Dynamics of lithospheric thinning and mantle melting by edge-driven convection: Application to Moroccan Atlas mountains, *Geochemistry, Geophysics, Geosystems*, *15*(8), 3175-3189.

Kameyama, M., & Nishioka, R. (2012), Generation of ascending flows in the Big Mantle Wedge (BMW) beneath northeast Asia induced by retreat and stagnation of subducted slab, *Geophysical Research Letters*, *39*(10).

Karato, S.-i., Riedel, M. R., & Yuen, D. A. (2001), Rheological structure and deformation of subducted slabs in the mantle transition zone: implications for mantle circulation and deep earthquakes, *Physics of the Earth and Planetary Interiors*, *127*(1-4), 83-108.

Katz, R. F., Spiegelman, M., & Langmuir, C. H. (2003), A new parameterization of hydrous mantle melting, *Geochemistry, Geophysics, Geosystems*, *4*(9).

Kaufmann, G., & Lambeck, K. (2000), Mantle dynamics, postglacial rebound and the radial viscosity profile, *Physics of the Earth and Planetary Interiors*, *121*(3), 301-324.

Kelemen, P., Hirth, G., Shimizu, N., Spiegelman, M., & Dick, H. (1997), A review of melt migration processes in the adiabatically upwelling mantle beneath oceanic spreading ridges, *Philosophical Transactions of the Royal Society of London A: Mathematical, Physical and Engineering Sciences*, *355*(1723), 283-318.

Keppler, H. (1996), Constraints from partitioning experiments on the composition of subduction-zone fluids, *Nature*, *380*(6571), 237.

Kim, S.-S., & Wessel, P. (2015), Finding seamounts with altimetry-derived gravity data. paper presented at OCEANS'15 MTS/IEEE Washington, IEEE.

King, S. D., & Masters, G. (1992), An inversion for radial viscosity structure using seismic tomography, *Geophysical Research Letters*, *19*(15), 1551-1554.

King, S. D., & Anderson, D. L. (1995), An alternative mechanism of flood basalt formation, *Earth and Planetary Science Letters*, *136*(3-4), 269-279.

King, S. D., & Ritsema, J. (2000), African hot spot volcanism: small-scale convection in the upper mantle beneath cratons, *Science*, *290*(5494), 1137-1140.

Kogiso, T., Tatsumi, Y., & Nakano, S. (1997), Trace element transport during dehydration processes in the subducted oceanic crust: 1. Experiments and implications for the origin of ocean island basalts, *Earth and Planetary Science Letters*, *148*(1-2), 193-205.

Kogiso, T., Tatsumi, Y., Shimoda, G., & Barsczus, H. G. (1997), High μ (HIMU) ocean island basalts in southern Polynesia: New evidence for whole mantle scale recycling of subducted oceanic crust, *Journal of Geophysical Research: Solid Earth*, *102*(B4), 8085-8103.

Kohlstedt, D., Keppler, H., & Rubie, D. (1996), Solubility of water in the α, β and γ phases of (Mg, Fe) 2 SiO 4, *Contributions to Mineralogy and Petrology*, *123*(4), 345-357.

Komabayashi, T. (2006), Phase relations of hydrous peridotite: implications for water circulation in the Earth's mantle, *GEOPHYSICAL MONOGRAPH-AMERICAN GEOPHYSICAL UNION*, *168*, 29.

Kuritani, T., Ohtani, E., & Kimura, J.-I. (2011), Intensive hydration of the mantle transition zone beneath China caused by ancient slab stagnation, *Nature Geoscience*, *4*(10), 713-716.

Kuritani, T., Kimura, J.-I., Ohtani, E., Miyamoto, H., & Furuyama, K. (2013), Transition zone origin of potassic basalts from Wudalianchi volcano, northeast China, *Lithos*, *156-159*, 1-12.

Lambart, S., Baker, M. B., & Stolper, E. M. (2016), The role of pyroxenite in basalt genesis: Melt‐PX, a melting parameterization for mantle pyroxenites between 0.9 and 5 GPa, *Journal of Geophysical Research*, *121*(8).

Leahy, G. M., & Bercovici, D. (2007), On the dynamics of a hydrous melt layer above the transition zone, *Journal of Geophysical Research*, *112*(B7).

Lei, J., & Zhao, D. (2005), P-wave tomography and origin of the Changbai intraplate volcano in Northeast Asia, *Tectonophysics*, *397*(3-4), 281-295.

Li, H.-Y., Xu, Y.-G., Ryan, J. G., Huang, X.-L., Ren, Z.-Y., Guo, H., & Ning, Z.-G. (2016), Olivine and melt inclusion chemical constraints on the source of intracontinental basalts from the eastern North China Craton: Discrimination of contributions from the subducted Pacific slab, *Geochimica et Cosmochimica Acta*, *178*, 1-19.

Liao, J., Wang, Q., Gerya, T., & Ballmer, M. D. (2017), Modeling Craton Destruction by Hydration-Induced Weakening of the Upper Mantle, *Journal of Geophysical Research: Solid Earth*, *122*(9), 7449-7466.

Lipman, P. W., & Glazner, A. F. (1991), Introduction to Middle Tertiary Cordilleran Volcanism: Magma Sources and Relations to Regional Tectonics, *Journal of Geophysical Research: Solid Earth*, *96*(B8), 13193-13199.

Liu, J., Han, J., & Fyfe, W. S. (2001), Cenozoic episodic volcanism and continental rifting in northeast China and possible link to Japan Sea development as revealed from K–Ar geochronology, *Tectonophysics*, *339*(3-4), 385-401.

Liu, J., Xia, Q.-K., Deloule, E., Chen, H., & Feng, M. (2015), Recycled oceanic crust and marine sediment in the source of alkali basalts in Shandong, eastern China: Evidence from magma water content and oxygen isotopes, *Journal of Geophysical Research: Solid Earth*, *120*(12), 8281-8303.

Liu, L., & Stegman, D. R. (2011), Segmentation of the Farallon slab, *Earth and Planetary Science Letters*, *311*(1-2), 1-10.

Liu, L., & Stegman, D. R. (2012), Origin of Columbia River flood basalt controlled by propagating rupture of the Farallon slab, *Nature*, *482*(7385), 386-389.

Liu, X., Zhao, D., Li, S., & Wei, W. (2017), Age of the subducting Pacific slab beneath East Asia and its geodynamic implications, *Earth and Planetary Science Letters*, *464*, 166-174.

Long, M. D., & Silver, P. G. (2008), The subduction zone flow field from seismic anisotropy: A global view, *science*, *319*(5861), 315-318.

Lustrino, M., & Wilson, M. (2007), The circum-Mediterranean anorogenic Cenozoic igneous province, *Earth-Science Reviews*, *81*(1-2), 1-65.

Madsen, J. K., Thorkelson, D. J., Friedman, R. M., & Marshall, D. D. (2006), Cenozoic to Recent plate configurations in the Pacific Basin: Ridge subduction and slab window magmatism in western North America, *Geosphere*, *2*(1), 11.

Marschall, H. R., & Schumacher, J. C. (2012), Arc magmas sourced from mélange diapirs in subduction zones, *Nature Geoscience*, *5*(12), 862-867.

Maruyama, S., Hasegawa, A., Santosh, M., Kogiso, T., Omori, S., Nakamura, H., Kawai, K., & Zhao, D. (2009), The dynamics of big mantle wedge, magma factory, and metamorphic–metasomatic factory in subduction zones, *Gondwana Research*, *16*(3-4), 414-430.

Matsuno, T., et al. (2017), Mantle transition zone beneath a normal seafloor in the northwestern Pacific: Electrical conductivity, seismic thickness, and water content, *Earth and Planetary Science Letters*, *462*, 189-198.

Mazza, S. E., Gazel, E., Bizimis, M., Moucha, R., Beguelin, P., Johnson, E. A., McAleer, R. J., & Sobolev, A. V. (2019), Sampling the volatile-rich transition zone beneath Bermuda, *Nature*, *569*(7756), 398-403.

McDonough, W. F., & Sun, S. s. (1995), The composition of the Earth, *Chemical Geology*, *120*(3-4), 223-253.

McKenzie, D. (1985), The extraction of magma from the crust and mantle, *Earth and Planetary Science Letters*, *74*(1), 81-91.

McKenzie, D., & Bickle, M. J. (1990), A eutectic parameterization of mantle melting, *Journal of Physics of the Earth*, *38*(6), 511-515.

McNutt, M. K. (1998), Superswells, *Reviews of Geophysics*, *36*(2), 211-244.

Mei, S., Bai, W., Hiraga, T., & Kohlstedt, D. (2002), Influence of melt on the creep behavior of olivine–basalt aggregates under hydrous conditions, *Earth and Planetary Science Letters*, *201*(3-4), 491-507.

Merle, O., & Michon, L. (2001), The formation of the West European Rift; a new model as exemplified by the Massif Central area, *Bulletin de la Société Géologique de France*, *172*(2), 213-221.

Miller, M. S., Gorbatov, A., & Kennett, B. L. N. (2006), Three-dimensional visualization of a near-vertical slab tear beneath the southern Mariana arc, *Geochemistry, Geophysics, Geosystems*, *7*(6), n/a-n/a.

Mitrovica, J. X., & Forte, A. M. (1997), Radial profile of mantle viscosity: Results from the joint inversion of convection and postglacial rebound observables, *Journal of Geophysical Research: Solid Earth*, *102*(B2), 2751-2769.

Moresi, L., Zhong, S., & Gurnis, M. (1996), The accuracy of finite element solutions of Stokes's flow with strongly varying viscosity, *Physics of the Earth and Planetary Interiors*, *97*(1-4), 83-94.

Morgan, W. J. (1971), Convection plumes in the lower mantle, *Nature*, *230*(5288), 42.

Morgan, W. J. (1972), Deep mantle convection plumes and plate motions, *AAPG bulletin*, *56*(2), 203-213.

Motoki, M. H., & Ballmer, M. D. (2015), Intraplate volcanism due to convective instability of stagnant slabs in the mantle transition zone, *Geochemistry, Geophysics, Geosystems*, *16*(2), 538-551.

Murakami, M., Hirose, K., Yurimoto, H., Nakashima, S., & Takafuji, N. (2002), Water in Earth's lower mantle, *Science*, *295*(5561), 1885-1887.

Nakagawa, T. (2017), On the numerical modeling of the deep mantle water cycle in global-scale mantle dynamics: The effects of the water solubility limit of lower mantle minerals, *Journal of Earth Science*, *28*(4), 563-577.

Nakagawa, T., & Buffett, B. A. (2005), Mass transport mechanism between the upper and lower mantle in numerical simulations of thermochemical mantle convection with multicomponent phase changes, *Earth & Planetary Science Letters*, *230*(1-2), 11-27.

Nelson, P. L., & Grand, S. P. (2018), Lower-mantle plume beneath the Yellowstone hotspot revealed by core waves, *Nature Geoscience*, *11*(4), 280-284.

Nishi, M., Irifune, T., Tsuchiya, J., Tange, Y., Nishihara, Y., Fujino, K., & Higo, Y. (2014), Stability of hydrous silicate at high pressures and water transport to the deep lower mantle, *Nature Geoscience*, *7*(3), 224-227.

O'Connor, J. M., & Duncan, R. A. (1990), Evolution of the Walvis Ridge-Rio Grande Rise Hot Spot System: Implications for African and South American Plate motions over plumes, *Journal of Geophysical Research*, *95*(B11), 17475.

Ohira, I., Ohtani, E., Sakai, T., Miyahara, M., Hirao, N., Ohishi, Y., & Nishijima, M. (2014), Stability of a hydrous δ-phase, AlOOH–MgSiO2(OH)2, and a mechanism for water transport into the base of lower mantle, *Earth and Planetary Science Letters*, *401*, 12-17.

Ohtani, E. (2005), Water in the mantle, *Elements*, *1*(1), 25-30.

Ohtani, E., & Maeda, M. (2001), Density of basaltic melt at high pressure and stability of the melt at the base of the lower mantle, *Earth and Planetary Science Letters*, *193*(1-2), 69-75.

Ohtani, E., Nagata, Y., Suzuki, A., & Kato, T. (1995), Melting relations of peridotite and the density crossover in planetary mantles, *Chemical Geology*, *120*(3-4), 207-221.

Ohtani, E., Litasov, K., Hosoya, T., Kubo, T., & Kondo, T. (2004), Water transport into the deep mantle and formation of a hydrous transition zone, *Physics of the Earth and Planetary Interiors*, *143-144*, 255-269.

Okal, E. A., & Batiza, R. (1987), Hotspots: The first 25 years, *Seamounts, Islands, and Atolls, Geophys. Monogr. Ser*, *43*, 1-10.

Panero, W. R. (2010), First principles determination of the structure and elasticity of hydrous ringwoodite, *Journal of Geophysical Research*, *115*(B3).

Parsons, B., & McKenzie, D. (1978), Mantle convection and the thermal structure of the plates, *Journal of Geophysical Research*, *83*(B9), 4485.

Pearson, D. G., et al. (2014), Hydrous mantle transition zone indicated by ringwoodite included within diamond, *Nature*, *507*(7491), 221-224.

Peltier, W. R. (1996), Mantle viscosity and ice-age ice sheet topography, *Science*, *273*(5280), 1359-1364.

Pertermann, M., & Hirschmann, M. M. (2003), Anhydrous partial melting experiments on MORB-like eclogite: phase relations, phase compositions and mineral–melt partitioning of major elements at 2–3 GPa, *Journal of Petrology*, *44*(12), 2173-2201.

Pierce, K. L., Morgan, L. A., & Link, P. (1992), The track of the Yellowstone hot spot: Volcanism, faulting, and uplift, *Regional geology of eastern Idaho and western Wyoming: Geological Society of America Memoir*, *179*(322), 1-53.

Piromallo, C., & Morelli, A. (2003), Pwave tomography of the mantle under the Alpine-Mediterranean area, *Journal of Geophysical Research: Solid Earth*, *108*(B2).

Pollitz, F. F., Wicks, C., & Thatcher, W. (2001), Mantle flow beneath a continental strike-slip fault: Postseismic deformation after the 1999 Hector Mine earthquake, *Science*, *293*(5536), 1814-1818.

Prelević, D., Foley, S. F., Romer, R., & Conticelli, S. (2008), Mediterranean Tertiary lamproites derived from multiple source components in postcollisional geodynamics, *Geochimica et Cosmochimica Acta*, *72*(8), 2125-2156.

Raddick, M. J., Parmentier, E. M., & Scheirer, D. S. (2002), Buoyant decompression melting: A possible mechanism for intraplate volcanism, *Journal of Geophysical Research: Solid Earth*, *107*(B10), ECV 7-1-ECV 7-14.

Ren, J., Tamaki, K., Li, S., & Junxia, Z. (2002), Late Mesozoic and Cenozoic rifting and its dynamic setting in Eastern China and adjacent areas, *Tectonophysics*, *344*(3-4), 175-205.

Revenaugh, J., & Sipkin, S. (1994), Seismic evidence for silicate melt atop the 410-km mantle discontinuity, *Nature*, *369*(6480), 474.

Richard, G. C., & Bercovici, D. (2009), Water-induced convection in the Earth's mantle transition zone, *Journal of Geophysical Research: Solid Earth*, *114*(B1).

Richard, G. C., & Iwamori, H. (2010), Stagnant slab, wet plumes and Cenozoic volcanism in East Asia, *Physics of the Earth and Planetary Interiors*, *183*(1-2), 280-287.

Riedel, M. R., & Karato, S.-i. (1997), Grain-size evolution in subducted oceanic lithosphere associated with the olivine-spinel transformation and its effects on rheology, *Earth and Planetary Science Letters*, *148*(1-2), 27-43.

Ringwood, A. E. (1975), Composition and Petrology of the Earth's Mantle, *MacGraw-Hill*, *618*.

Ritter, J. R. R., Jordan, M., Christensen, U. R., & Achauer, U. (2001), A mantle plume below the Eifel volcanic fields, Germany, *Earth and Planetary Science Letters*, *186*(1), 7-14.

Rosenbaum, G., Gasparon, M., Lucente, F. P., Peccerillo, A., & Miller, M. S. (2008), Kinematics of slab tear faults during subduction segmentation and implications for Italian magmatism, *Tectonics*, *27*(2), n/a-n/a.

Rudolph, M. L., Lekić, V., & Lithgow-Bertelloni, C. (2015), Viscosity jump in Earth's mid-mantle, *Science*, *350*(6266), 1349-1352.

Rudzitis, S., Reid, M. R., & Blichert-Toft, J. (2016), On edge melting under the Colorado Plateau margin, *Geochemistry, Geophysics, Geosystems*, *17*(7), 2835-2854.

Schmandt, B., & Lin, F. C. (2014), P and S wave tomography of the mantle beneath the United States, *Geophysical Research Letters*, *41*(18), 6342-6349.

Schmeling, H. (2006), A model of episodic melt extraction for plumes, *Journal of Geophysical Research: Solid Earth*, *111*(B3), n/a-n/a.

Sigloch, K., McQuarrie, N., & Nolet, G. (2008), Two-stage subduction history under North America inferred from multiple-frequency tomography, *Nature Geoscience*, *1*(7), 458-462.

Smithies, R. H., Champion, D. C., & Cassidy, K. F. (2003), Formation of Earth's early Archaean continental crust, *Precambrian Research*, *127*(1-3), 89-101.

Solomatov, V. S., & Moresi, L. N. (2000), Scaling of time-dependent stagnant lid convection: Application to small-scale convection on Earth and other terrestrial planets, *Journal of Geophysical Research: Solid Earth*, *105*(B9), 21795-21817.

Song, T.-R. A., Helmberger, D. V., & Grand, S. P. (2004), Low-velocity zone atop the 410-km seismic discontinuity in the northwestern United States, *Nature*, *427*(6974), 530.

Stracke, A., Bourdon, B., & McKenzie, D. (2006), Melt extraction in the Earth's mantle: constraints from U–Th–Pa–Ra studies in oceanic basalts, *Earth and Planetary Science Letters*, *244*(1-2), 97-112.

Tackley, P., & Stevenson, D. (1993), A mechanism for spontaneous self-perpetuating volcanism on the terrestrial planets, in *Flow and Creep in the Solar System: Observations, Modeling and Theory*, edited, pp. 307-321, Springer.

Takahahshi, E., Nakajima, K., & Wright, T. L. (1998), Origin of the Columbia River basalts: melting model of a heterogeneous plume head, *Earth and Planetary Science Letters*, *162*(1-4), 63-80.

Tan, E., & Gurnis, M. (2005), Metastable superplumes and mantle compressibility, *Geophysical Research Letters*, *32*(20).

Tang, Y., Obayashi, M., Niu, F., Grand, S. P., Chen, Y. J., Kawakatsu, H., Tanaka, S., Ning, J., & Ni, J. F. (2014), Changbaishan volcanism in northeast China linked to subduction-induced mantle upwelling, *Nature Geoscience*, *7*(6), 470-475.

Tatsumi, Y., Maruyama, S., & Nohda, S. (1990), Mechanism of backarc opening in the Japan Sea: role of asthenospheric injection, *Tectonophysics*, *181*(1-4), 299-306.

Tauzin, B., Debayle, E., & Wittlinger, G. (2010), Seismic evidence for a global low-velocity layer within the Earth’s upper mantle, *Nature Geoscience*, *3*(10), 718-721.

Thorkelson, D. J. (1996), Subduction of diverging plates and the principles of slab window formation, *Tectonophysics*, *255*(1-2), 47-63.

Till, C. B., Elkins-Tanton, L. T., & Fischer, K. M. (2010), A mechanism for low-extent melts at the lithosphere-asthenosphere boundary, *Geochemistry, Geophysics, Geosystems*, *11*(10), n/a-n/a.

Tosi, N., Yuen, D. A., de Koker, N., & Wentzcovitch, R. M. (2013), Mantle dynamics with pressure- and temperature-dependent thermal expansivity and conductivity, *Physics of the Earth and Planetary Interiors*, *217*, 48-58.

Valentine, G. A., & Hirano, N. (2010), Mechanisms of low-flux intraplate volcanic fields—Basin and Range (North America) and northwest Pacific Ocean, *Geology*, *38*(1), 55-58.

van der Lee, S., Regenauer-Lieb, K., & Yuen, D. A. (2008), The role of water in connecting past and future episodes of subduction, *Earth and Planetary Science Letters*, *273*(1-2), 15-27.

van Hunen, J., Zhong, S., Shapiro, N., & Ritzwoller, M. (2005), New evidence for dislocation creep from 3-D geodynamic modeling of the Pacific upper mantle structure, *Earth and Planetary Science Letters*, *238*(1-2), 146-155.

van Keken, P. E., Hacker, B. R., Syracuse, E. M., & Abers, G. A. (2011), Subduction factory: 4. Depth-dependent flux of H2O from subducting slabs worldwide, *Journal of Geophysical Research*, *116*(B1).

Veizer, J. (1989), Strontium isotopes in seawater through time, *Annual Review of Earth and Planetary Sciences*, *17*(1), 141-167.

Vollmer, R., Ogden, P., Schilling, J.-G., Kingsley, R. H., & Waggoner, D. G. (1984), Nd and Sr isotopes in ultrapotassic volcanic rocks from the Leucite Hills, Wyoming, *Contributions to Mineralogy and Petrology*, *87*(4), 359-368.

Wang, F., Zhou, X.-H., Zhang, L.-C., Ying, J.-F., Zhang, Y.-T., Wu, F.-Y., & Zhu, R.-X. (2006), Late Mesozoic volcanism in the Great Xing'an Range (NE China): Timing and implications for the dynamic setting of NE Asia, *Earth and Planetary Science Letters*, *251*(1-2), 179-198.

Wang, J., Sinogeikin, S. V., Inoue, T., & Bass, J. D. (2003), Elastic properties of hydrous ringwoodite, *American Mineralogist*, *88*(10), 1608-1611.

Wang, J., Sinogeikin, S. V., Inoue, T., & Bass, J. D. (2006), Elastic properties of hydrous ringwoodite at high-pressure conditions, *Geophysical Research Letters*, *33*(14).

Wang, X.-J., Chen, L.-H., Hofmann, A. W., Mao, F.-G., Liu, J.-Q., Zhong, Y., Xie, L.-W., & Yang, Y.-H. (2017), Mantle transition zone-derived EM1 component beneath NE China: Geochemical evidence from Cenozoic potassic basalts, *Earth and Planetary Science Letters*, *465*, 16-28.

Weaver, B. L. (1991), The origin of ocean island basalt end-member compositions: trace element and isotopic constraints, *Earth and Planetary Science Letters*, *104*(2-4), 381-397.

Wedepohl, K. H., & Baumann, A. (1999), Central European Cenozoic plume volcanism with OIB characteristics and indications of a lower mantle source, *Contributions to Mineralogy and Petrology*, *136*(3), 225-239.

Wellman, P., & McDougall, I. (1974), Potassium ‐ argon ages on the Cainozoic volcanic rocks of New South Wales, *Journal of the Geological Society of Australia*, *21*(3), 247-272.

West, J. D., Fouch, M. J., Roth, J. B., & Elkins-Tanton, L. T. (2009), Vertical mantle flow associated with a lithospheric drip beneath the Great Basin, *Nature Geoscience*, *2*(6), 439-444.

Wilson, J. T. (1965), Evidence from ocean islands suggesting movement in the earth, *Phil. Trans. R. Soc. Lond. A*, *258*(1088), 145-167.

Wilson, J. T. (1973), Mantle plumes and plate motions, *Tectonophysics*, *19*(2), 149-164.

Wilson, M., & Downes, H. (2005), Tertiary-Quaternary intra-plate magmatism in Europe and its relationship to mantle dynamics.

Wilson, M., & Downes, H. (2006), Tertiary-Quaternary intra-plate magmatism in Europe and its relationship to mantle dynamics, *Geological Society, London, Memoirs*, *32*(1), 147-166.

Windley, B. F., & Xiao, W. (2018), Ridge subduction and slab windows in the Central Asian Orogenic Belt: Tectonic implications for the evolution of an accretionary orogen, *Gondwana Research*, *61*, 73-87.

Xu, W., Lithgow-Bertelloni, C., Stixrude, L., & Ritsema, J. (2008), The effect of bulk composition and temperature on mantle seismic structure, *Earth and Planetary Science Letters*, *275*(1-2), 70-79.

Yan, J., & Zhao, J.-X. (2008), Cenozoic alkali basalts from Jingpohu, NE China: The role of lithosphere–asthenosphere interaction, *Journal of Asian Earth Sciences*, *33*(1-2), 106-121.

Yu, S.-Y., Xu, Y.-G., Zhou, S.-H., Lan, J.-B., Chen, L.-M., Shen, N.-P., Zhao, J.-X., & Feng, Y.-X. (2018), Late Cenozoic basaltic lavas from the Changbaishan-Baoqing

Volcanic Belt, NE China: Products of lithosphere-asthenosphere interaction induced by subduction of the Pacific plate, *Journal of Asian Earth Sciences*, *164*, 260-273.

Zeng, G., Chen, L.-H., Hofmann, A. W., Jiang, S.-Y., & Xu, X.-S. (2011), Crust recycling in the sources of two parallel volcanic chains in Shandong, North China, *Earth and Planetary Science Letters*, *302*(3-4), 359-368.

Zhang, M., Suddaby, P., Thompson, R. N., Thirlwall, M. F., & Menzies, M. A. (1995), Potassic volcanic rocks in NE China: geochemical constraints on mantle source and magma genesis, *Journal of Petrology*, *36*(5), 1275-1303.

Zhang, M., Stephenson, P. J., O'Reilly, S. Y., Mcculloch, M. T., & Norman, M. (2001), Petrogenesis and Geodynamic Implications of Late Cenozoic Basalts in North Queensland, Australia: Trace-element and Sr–Nd–Pb Isotope Evidence, *42*(4), 685-719(635).

Zhao, D. (2004), Origin of the Changbai intraplate volcanism in Northeast China: Evidence from seismic tomography, *Chinese Science Bulletin*, *49*(13), 1401.

Zhao, D., & Ohtani, E. (2009), Deep slab subduction and dehydration and their geodynamic consequences: Evidence from seismology and mineral physics, *Gondwana Research*, *16*(3-4), 401-413.

Zhao, D., Maruyama, S., & Omori, S. (2007), Mantle dynamics of Western Pacific and East Asia: Insight from seismic tomography and mineral physics, *Gondwana Research*, *11*(1-2), 120-131.

Zhong, S., Zuber, M. T., Moresi, L., & Gurnis, M. (2000), Role of temperature-dependent viscosity and surface plates in spherical shell models of mantle convection, *Journal of Geophysical Research: Solid Earth*, *105*(B5), 11063-11082.

Zindler, A., & Hart, S. (1986), Chemical geodynamics, *Annual review of earth and planetary sciences*, *14*(1), 493-571.

Zlotnik, S., Afonso, J. C., Díez, P., & Fernández, M. (2008), Small-scale gravitational instabilities under the oceans: Implications for the evolution of oceanic lithosphere and its expression in geophysical observables, *Philosophical Magazine*, *88*(28-29), 3197-3217.

Zou, H., Fan, Q., & Yao, Y. (2008), U–Th systematics of dispersed young volcanoes in NE China: Asthenosphere upwelling caused by piling up and upward thickening of stagnant Pacific slab, *Chemical Geology*, *255*(1-2), 134-142.

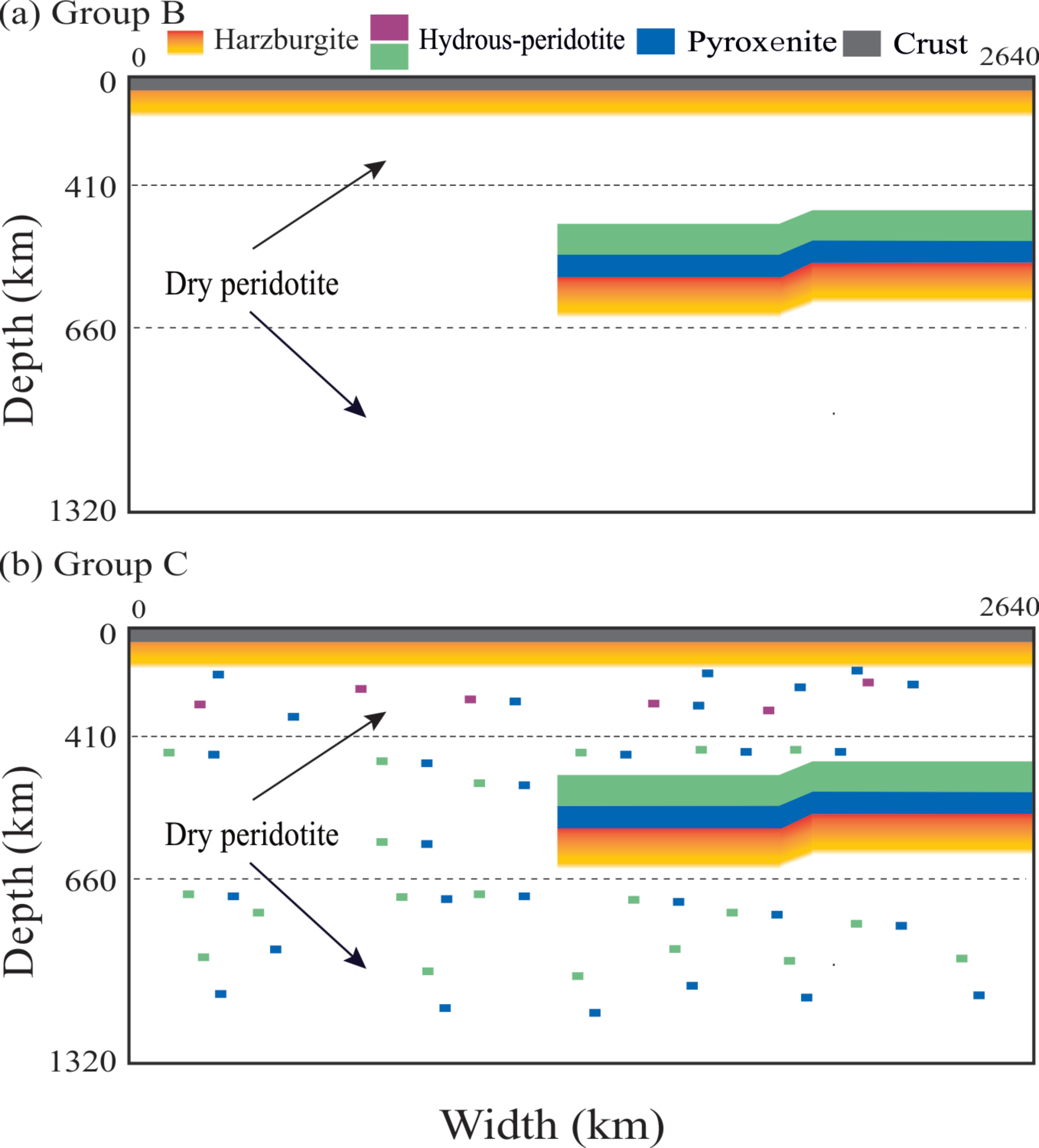
(a) Group B
Harzburgite
Hydrous-peridotite
Pyroxenite
Crust
0
2640
0
410
660
1320
Dry peridotite
Depth (km)
(b) Group C
0
2640
0
410
660
1320
Dry peridotite
Depth (km)
Width (km)

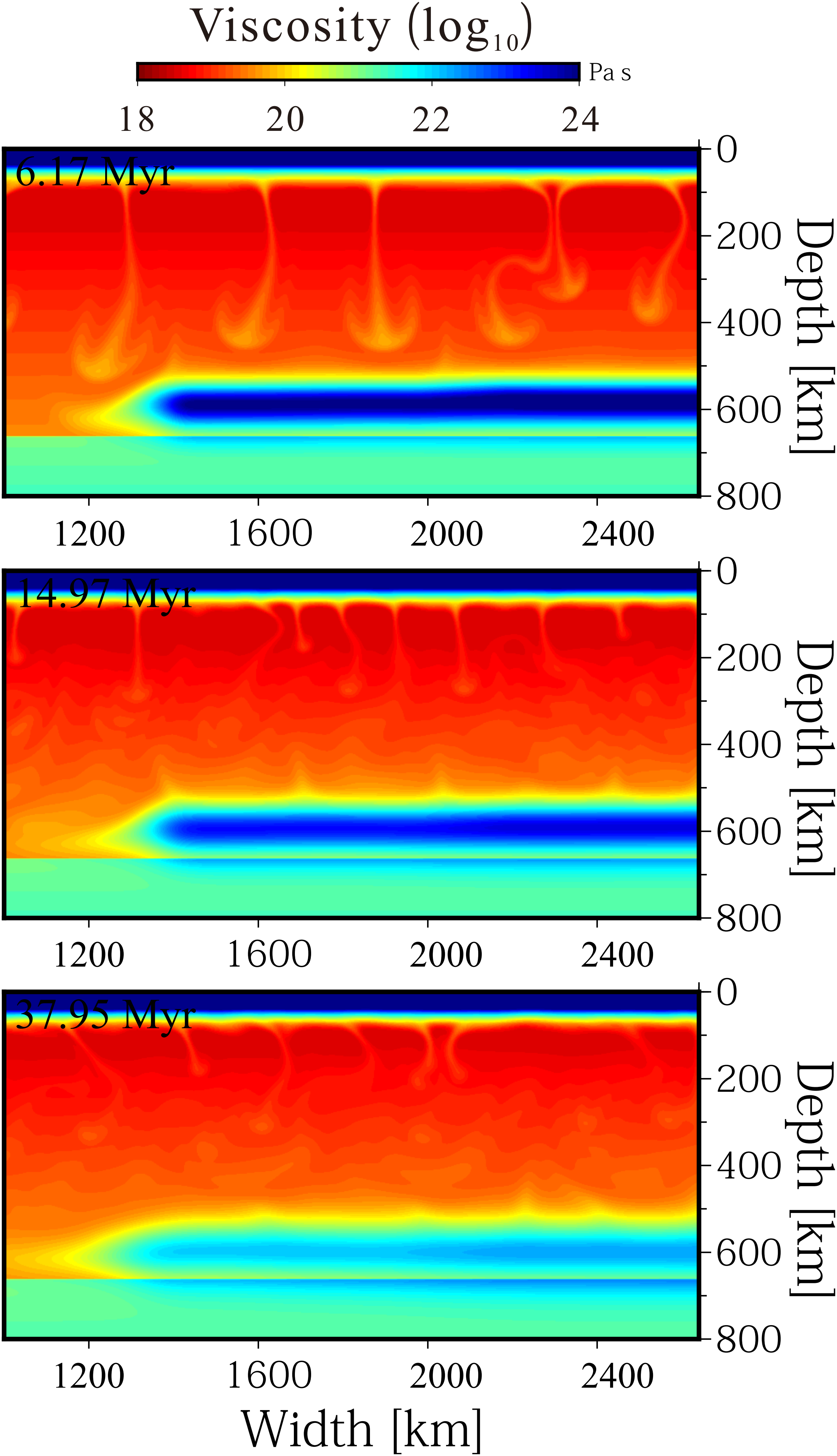

Viscosity ($\log_{10}$)
Pa s
18
20
22
24
6.17 Myr
14.97 Myr
37.95 Myr
0
200
400
600
800
Depth [km]
1200
1600
2000
2400
Width [km]

Table S2. Summary of the results of Group B and C

Case	Model Parameters						Model Predictions			
	η_{eff} ($\times 10^{18}$ Pa s)	C_{H2O_HP} (ppm)	D_{HP} （km）	χ_{PX} (ambient mantle)	Slab age		τ_u (Myr)	τ_m (Myr)	V_{melt} (m^2)	Pyroxenite Contribution
					Left (Myr)	Right (Myr)				
B11	2.2	4000	60	0.0	70	80	2.64	7.39	2.3483	0.0000
B12	6.25	4000	60	0.0	70	80	7.27	18.71	0.0219	0.0000
B13	11.0	4000	60	0.0	70	80	11.83	32.84	0.0001	0.0000
B21	3.75	400	60	0.0	70	80	8.89	26.81	0.0117	0.0000
B22	3.75	2000	60	0.0	70	80	7.07	17.95	0.0610	0.0000
B23	3.75	6000	60	0.0	70	80	4.48	11.70	0.1826	0.0000
B24	3.75	8000	60	0.0	70	80	1.83	10.10	0.2396	0.0000
B25	3.75	10000	60	0.0	70	80	0.93	14.13	0.2871	0.0000
B31	3.75	4000	10	0.0	70	80	/	/	/	/
B32	3.75	4000	30	0.0	70	80	/	/	/	/
B33	3.75	4000	50	0.0	70	80	9.18	20.92	0.0140	0.0000
B34	3.75	4000	80	0.0	70	80	0.03	7.36	1.1387	0.0000
B35	3.75	4000	135	0.0	70	80	0.00	5.20	3.1768	0.0000
B41	3.75	4000	60	0.0	5	5	11.83	32.84	0.0001	0.0000
B42	3.75	4000	60	0.0	20	20	5.33	11.25	0.0794	0.0000
B43	3.75	4000	60	0.0	50	50	5.54	12.08	0.2450	0.0001
B44	3.75	4000	60	0.0	70	70	4.98	11.48	0.0690	0.0000
B45	3.75	4000	60	0.0	90	90	4.50	12.06	0.1334	0.0000
B51	3.75	4000	60	0.0	5	15	4.25	12.01	0.1076	0.0000
B52	3.75	4000	60	0.0	20	30	7.01	9.42	0.4400	0.0017
B53	3.75	4000	60	0.0	50	60	5.62	11.80	0.2277	0.0004
B54	3.75	4000	60	0.0	80	90	4.93	12.06	0.2309	0.0000
B61	3.75	4000	60	0.0	70	60	4.36	11.99	0.1454	0.0000
B62	3.75	4000	60	0.0	70	65	4.50	11.31	0.2860	0.0000
B63	3.75	4000	60	0.0	70	68	4.50	11.30	0.1369	0.0003
B64	3.75	4000	60	0.0	70	73	4.50	12.12	0.0599	0.0000
B65	3.75	4000	60	0.0	70	75	4.50	11.59	0.2379	0.0000
C11	2.2	4000	60	0.01	70	80	2.64	2.44	32.7001	0.9273
C12	6.25	4000	60	0.01	70	80	7.27	7.40	3.7330	0.9470
C13	11.0	4000	60	0.01	70	80	11.85	10.68	1.1717	0.9566
C21	3.75	400	60	0.01	70	80	8.71	4.32	14.9916	0.9541
C22	3.75	2000	60	0.01	70	80	6.22	4.25	14.5092	0.9497
C23	3.75	6000	60	0.01	70	80	4.47	4.31	14.2920	0.9413
C24	3.75	8000	60	0.01	70	80	1.73	4.20	13.7842	0.9296
C25	3.75	10000	60	0.01	70	80	0.82	4.01	15.1212	0.9427
C26	3.75	4000	60	0.001	70	80	4.49	4.32	2.2744	0.6352
C31	3.75	4000	10	0.01	70	80	/	4.32	14.2036	0.9568
C32	3.75	4000	30	0.01	70	80	/	4.34	14.5843	0.9561

C33	3.75	4000	50	0.01	70	80	8.85	4.23	14.6201	0.9537
C34	3.75	4000	80	0.01	70	80	0.12	3.76	15.08	0.8829
C35	3.75	4000	135	0.01	70	80	0	2.89	18.1007	0.7328
C41	3.75	4000	60	0.01	5	5	5.35	4.04	17.9563	0.8902
C42	3.75	4000	60	0.01	20	20	5.42	4.20	16.4362	0.9355
C43	3.75	4000	60	0.01	50	50	4.76	4.25	15.5509	0.9418
C44	3.75	4000	60	0.01	70	70	4.49	4.35	14.9027	0.9496
C45	3.75	4000	60	0.01	90	90	4.25	4.19	14.9844	0.9487
C51	3.75	4000	60	0.01	5	15	4.57	4.19	16.7789	0.9164
C52	3.75	4000	60	0.01	20	30	5.12	4.23	16.0238	0.9368
C53	3.75	4000	60	0.01	50	60	4.73	4.27	15.3602	0.9327
C54	3.75	4000	60	0.01	80	90	4.36	4.28	14.3129	0.9396
C61	3.75	4000	60	0.01	70	60	4.49	4.37	14.2553	0.9304
C62	3.75	4000	60	0.01	70	65	4.49	4.37	13.9875	0.9443
C63	3.75	4000	60	0.01	70	68	4.49	4.37	14.3242	0.9493
C64	3.75	4000	60	0.01	70	73	4.49	4.35	14.3135	0.9320
C65	3.75	4000	60	0.01	70	75	4.49	4.36	14.8259	0.9457

/ No data acquired within 70 Myr

Table S1. Summary of the results of Group A (case 13 is the reference case)

	Model Parameters						Model Predictions			
Case	η_{eff} ($\times 10^{18}$ Pa s)	C_{H2O_HP} (ppm)	D_{HP} (km)	χ_{PX} (HP layer)	Slab age left (Myr)	Slab age right (Myr)	τ_u (Myr)	τ_m (Myr)	V_{melt} (m^2)	PX Contri-bution
11	2.2	4000	60	0.02	70	80	3.03	7.70	1.1328	0.4622
12	2.5	4000	60	0.02	70	80	3.62	8.55	0.6745	0.5289
13	3.75	4000	60	0.02	70	80	4.98	11.80	0.1802	0.5682
14	5.0	4000	60	0.02	70	80	7.11	15.76	0.0534	0.5552
15	6.25	4000	60	0.02	70	80	9.77	20.00	0.0097	0.6366
16	8.8	4000	60	0.02	70	80	13.83	31.16	0.0027	0.4698
17	11.0	4000	60	0.02	70	80	16.72	47.14	0.0000	1.0000
21	3.75	400	60	0.02	70	80	11.62	28.17	0.0276	0.5168
22	3.75	1000	60	0.02	70	80	9.52	17.86	0.0184	0.5438
23	3.75	2000	60	0.02	70	80	9.06	29.63	0.0158	0.6497
24	3.75	3000	60	0.02	70	80	6.08	15.84	0.0863	0.5685
25	3.75	5000	60	0.02	70	80	4.15	11.77	0.2650	0.5300
26	3.75	6000	60	0.02	70	80	2.05	10.80	0.2343	0.5312
27	3.75	8000	60	0.02	70	80	1.23	16.61	0.1861	0.6093
28	3.75	10000	60	0.02	70	80	0.85	12.37	0.1644	0.5870
31	3.75	4000	20	0.02	70	80	/	/	/	/
32	3.75	4000	40	0.02	70	80	/	/	/	/
33	3.75	4000	50	0.02	70	80	14.57	44.69	0.0078	0.5360
34	3.75	4000	70	0.02	70	80	2.53	10.44	0.4207	0.5604
35	3.75	4000	80	0.02	70	80	0.85	11.54	0.6451	0.5363
36	3.75	4000	90	0.02	70	80	0.05	9.84	0.9223	0.5306
37	3.75	4000	135	0.02	70	80	0.00	7.76	3.4309	0.5083
41	3.75	4000	60	0.00	70	80	4.48	11.70	0.1826	0.0000
42	3.75	4000	60	0.005	70	80	4.49	11.84	0.1840	0.2373
43	3.75	4000	60	0.01	70	80	4.95	12.17	0.2472	0.3605
44	3.75	4000	60	0.015	70	80	4.95	11.92	0.2296	0.4824
45	3.75	4000	60	0.03	70	80	5.32	11.93	0.2477	0.6124
46	3.75	4000	60	0.03	70	80	5.42	12.15	0.1339	0.6559
47	3.75	4000	60	0.035	70	80	5.61	12.39	0.1566	0.7224
48	3.75	4000	60	0.04	70	80	5.82	12.60	0.1269	0.7197
49	3.75	4000	60	0.045	70	80	6.03	12.83	0.1962	0.7619
410	3.75	4000	60	0.05	70	80	6.08	16.43	0.1131	0.7958
51	3.75	4000	60	0.02	5	5	5.92	14.50	0.3307	0.5380
52	3.75	4000	60	0.02	15	15	6.05	18.12	0.2468	0.6264
53	3.75	4000	60	0.02	20	20	6.00	13.33	0.1922	0.5309
54	3.75	4000	60	0.02	30	30	5.97	13.55	0.1781	0.5584
55	3.75	4000	60	0.02	50	50	5.61	15.41	0.2093	0.5384
56	3.75	4000	60	0.02	60	60	5.47	19.85	0.1603	0.6002

57	3.75	4000	60	0.02	70	70	5.21		13.63	0.1049	0.5880
58	3.75	4000	60	0.02	80	80	4.90		16.49	0.1370	0.5590
59	3.75	4000	60	0.02	90	90	4.77		12.18	0.1332	0.5521
61	3.75	4000	60	0.02	5	15	5.64	4.87*	11.45	0.3879	0.5545
62	3.75	4000	60	0.02	15	25	5.83	5.33*	16.05	0.3136	0.5331
63	3.75	4000	60	0.02	20	30	5.85	5.55*	17.22	0.2078	0.5639
64	3.75	4000	60	0.02	30	40	5.83	5.51*	12.26	0.3723	0.5265
65	3.75	4000	60	0.02	50	60	5.72	5.23*	13.14	0.2077	0.5856
66	3.75	4000	60	0.02	60	70	5.25	5.09*	12.44	0.2799	0.5334
67	3.75	4000	60	0.02	80	90	4.87	4.70*	12.05	0.2468	0.5253
71	3.75	4000	60	0.02	70	60	4.98	7.32*	12.53	0.1304	0.6193
72	3.75	4000	60	0.02	70	63	4.98	8.78*	12.84	0.1344	0.5679
73	3.75	4000	60	0.02	70	65	4.98	8.93*	17.91	0.1355	0.5699
74	3.75	4000	60	0.02	70	68	4.98	8.98*	17.21	0.1446	0.5796
75	3.75	4000	60	0.02	70	73	4.98	10.02*	13.39	0.0779	0.5848
76	3.75	4000	60	0.02	70	75	4.98	9.52*	12.55	0.1272	0.5318
77	3.75	4000	60	0.02	70	78	4.98	5.12*	12.49	0.1338	0.5501

/ No data acquired within 70 Myr

* Onset time of upwellings from near fracture zone.